Available online at www.sciencedirect.com
SCIENCE DIRECT®
Journal of Computational Physics 201 (2004) 344–375
JOURNAL OF COMPUTATIONAL PHYSICS
www.elsevier.com/locate/jcp

Multiphase semiclassical approximation of an electron in a one-dimensional crystalline lattice II. Impurities, confinement and Bloch oscillations ☆

Laurent Gosse

IAC–CNR "Mauro Picone" (sezione di Bari), Via Amendola 122/I, 70126 Bari, Italy

Received 7 October 2003; received in revised form 1 June 2004; accepted 1 June 2004
Available online 27 July 2004

Abstract

We present a computational approach for the WKB approximation of the wavefunction of an electron moving in a periodic one-dimensional crystal lattice by means of a nonstrictly hyperbolic system whose flux function stems from the Bloch spectrum of the Schrödinger operator. This second part focuses on the handling of the source terms which originate from adding a slowly varying exterior potential. Physically, relevant examples are the occurrence of Bloch oscillations in case it is linear, a quadratic one modelling a confining field and the harmonic Coulomb term resulting from the inclusion of a "donor impurity" inside an otherwise perfectly homogeneous lattice.

AMS: 81Q05; 81Q20; 35L65; 65M06

Keywords: Semiclassical limit; Periodic potential; Homogenization; Vlasov equation; Moment method; Nonstrictly hyperbolic systems

1. Introduction

This paper is the second part of a numerical study of semiclassical approximation of the motion of electrons in short-scale periodic potentials. More precisely, we start from the Schrödinger equation in one space dimension,

$$\mathrm{i}\hbar\partial_t\psi + \frac{\hbar^2}{2m}\partial_{xx}\psi = e(V(x) + V_e(\varepsilon x))\psi, \quad x \in \mathbb{R}, \tag{1}$$

☆ Partially supported by the EEC network #HPRN-CT-2002-00282, the "Modelling and Computations in Wave Propagation" contract #HPMD-CT-2001-00121 and the Wittgenstein 2000 Award of P.A. Markowich funded by the Austrian Research Fund FWF. Also support from the Wolfgang Pauli Institute (Wien) and the Austrian FWF project P14876 No. 4 is acknowledged.

E-mail addresses: irmalg23@area.area.ba.cnr.it, l.gosse@area.ba.cnr.it. (L. Gosse)

0021-9991/$ - see front matter
doi:10.1016/j.jcp.2004.06.004

with $\hbar$ the Planck's constant, m and e the electronic mass and charge and $V \in \mathbb{R}$ the periodic potential modeling the interaction with a lattice of ionic cores in one space dimension ($x \in \mathbb{R}$). The smooth and slowly varying external potential V_e stands usually for an applied electric field or a Coulomb interaction term. We first change to "atomic units" for which $\hbar = m = e = 1$. Then we introduce the dimensionless parameter ε as the microscopic–macroscopic ratio; we assume it small and track wave packets with a spatial spreading of the order of $1/\varepsilon$ (see Fig. 1). We recast (1) in macroscopic variables $x \mapsto x/\varepsilon$, $t \mapsto t/\varepsilon$ (i.e., we study $O(\varepsilon)$-wavelength solutions) and a scaled problem arises

$$i\varepsilon \partial_t \psi + \frac{\varepsilon^2}{2} \partial_{xx} \psi = V\left(\frac{x}{\varepsilon}\right)\psi + V_e(x)\psi, \qquad V(x + 2\pi) = V(x), \tag{2}$$

for which the (semiclassical) limit $\varepsilon \to 0$ is of special interest. We assumed the period to be 2π on the atomic lengthscale for the sake of simplicity only.

A crystal is a periodic array of atoms which can be described through a Bravais lattice; their periodical position is due to the nature of the bonding. In the binding process, neighbouring atoms share only a few outer electrons, while their cores remain fixed at their lattice sites (adiabatic approximation). We begin by neglecting possible impurities in the crystal (perfect crystal assumption); those shared electrons feel a periodic potential generated from the ionic cores, which periodicity match the lattice constant. The Bloch theorem [1,8] ensures that eigenstates corresponding to this Hamiltonian can be written in the so-called *Bloch wave form*, namely $\Psi_\kappa^n(y) = \exp(i\kappa y) z_\kappa^n(y)$, with the modulation z_κ^n having the same periodicity as the underlying lattice and κ being known as the crystal momentum. For each value of κ, one obtains a set of eigenvalues $E_n(\kappa)$ which constitutes the spectrum for an electron with a certain (crystal) momentum κ. As we vary n and κ, a discrete series of continuum intervals of possible values for the electron's energy is described. When ordered, they are usually referred to as the energy bands for the crystal and may be represented with κ taking values in the *first Brillouin zone* only, see Section 2.1 and [29]. Hence before going further, some classical definitions are to be recalled:

- The Bravais lattice for (1), (2) is $\Gamma = 2\pi\mathbb{Z}$; its primitive cell is $]0, 2\pi[$.
- The reciprocal lattice Γ' is the set of wave numbers κ for which plane waves $\exp(i\kappa x)$ have the same periodicity as the potential V; i.e., $\Gamma' = \mathbb{Z}$.
- The first Brillouin zone B is the Wigner–Seitz cell of the dual lattice Γ' made of all κ closer to zero than to any other dual lattice point; $B =]-\frac{1}{2}, \frac{1}{2}[$.

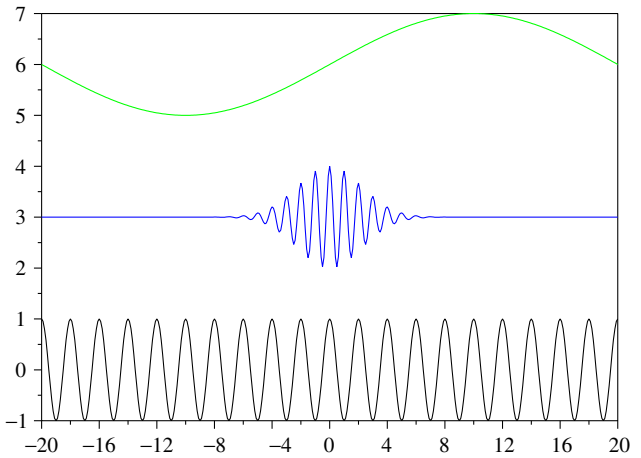

Fig. 1. Space scales for (1) and (2): the periodic potential, the wave packet and the exterior potential (bottom to top).

Electrons in a crystal fill the energy bands starting from the lowest one (core band) and at temperature $T = 0$, the highest occupied band is either completely or partially filled depending on the material under consideration. In the first case, no current can be transported and the crystal is an *insulator*; in the second one, charge carriers can flow and the material is a *metal*. The difference between the minimum of the first empty band and the maximum of the highest filled band is the *energy band gap* E_g (or simply "gap") and represents the minimum quantum of energy required to trigger an *interband transition*. When the temperature $T > 0$, electrons can move from the highest filled band towards the first empty one with a probability of the order of $\exp(-E_g/T)$ (see [1, Chapter 28]). Hence in case E_g is small enough, some electrons will tunnel into the first empty band and the material will become conducting at the ambient temperature; in this case, one speaks about *semiconductors*. The last completely filled band at $T = 0$ is called the *valence band* whereas the first empty one is the *conduction band*. In the ideal case and at low temperature, all the crystal's electrons sit in the valence band. The question is what happens if they get excited in some way (by an increase of the temperature, for instance, or by light photons). In case the exciting energy is big enough to overcome the band gap E_g, electrons will jump into the conduction band. It is erroneous to think that no transitions occur in the opposite case [1]. However, in this work, we shall focus on one-dimensional simulations during which interband transitions can generally be ignored. Bloch oscillations (BOs) is a well-known phenomenon discovered by Zener while studying the quantum properties of an electron in a (perfect) crystal submitted to a constant electric field [50] (see also [1,41]). The BO arises when a small spatial tilt is added to the lattice; quantum particles do not fall along the potential's slope but perform counterintuitive periodic oscillations. We shall call hereafter the untilted potential "lattice" and its sum with the applied field "tilted lattice" (see Fig. 2). Discrete systems such as semiconductor superlattices, molecular chains, waveguide arrays or atoms captured in optical potentials share the property of exhibiting BOs. For instance, if a static electric field is applied perpendicularly to the material layers in a superlattice, charged particles do not react on the electric force as could have been expected; an oscillating current is generated in contrast to the DC flow observed in bulk materials. This will be developed in Section 3.2. Laser cooling of atomic vapors has also brought interest to such problems which have been considered purely academic for long time [1]. Indeed, light potentials generated by standing waves have been used in many experimental studies of quantum dynamics and BOs have been observed both with single atoms and Bose–Einstein condensates in an accelerated standing wave. Placed in such a standing wave, an atom perceives a

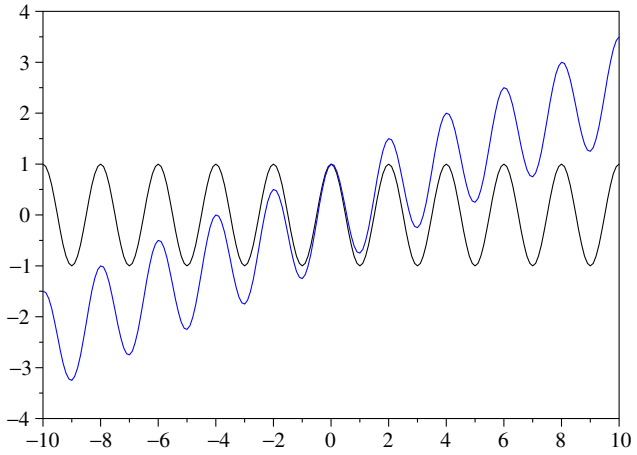

Fig. 2. Lattice and "tilted lattice".

periodic one-dimensional potential of the Mathieu's type while the gravity term provides the slowly varying linear tilt [23]. This case is to be investigated extensively within Section 3.3. Another case study of physical interest is the study of a confining field corresponding to a quadratic exterior potential; this is developed throughout Section 4.

The perfect crystal is only a mathematical idealization. Consider for instance the GaAs crystal; in reality, it is quite common to encounter atoms of Germanium inside the lattice. These impurities have an extra electron in the outer shell, so there is an extra fixed positive charge on some lattice sites together with an extra negative one wandering throughout the crystal. It is generally assumed that this "donor electron" feels a potential slightly different from the ideal crystal's one, namely an hydrogen-like equation can be derived [1]:

$$\left(E_n(\partial_x) + \frac{1}{\epsilon_0|x - x_{\text{impurity}}|}\right)\Psi(x) = E_{\text{extra } e^-}\Psi(x), \quad \epsilon_0 \simeq 16. \tag{3}$$

Generally, some of the corresponding energy levels lie inside the energy gap (see Section 5.1 for a simplified computation) and they can be narrowed in case the second derivative of the conduction band E_n is big for $\kappa \simeq 0$ (i.e., for a small effective mass). This leads to the concept of *hydrogenic donor*, which are shallow donors, i.e., donor impurities whose ionic core resembles the one of the atoms they stand for. However, even for certain deep donors that induce strongly localized perturbation in the crystal's potential, the lowest energy levels can still be described the same way, using the hydrogenic Hamiltonian; silicon is such an example. We shall model the presence of a donor impurity by means of the Coulomb interaction term inside (1):

$$V_{\text{e}}(x) = \frac{-e}{\epsilon_0|x - x_{\text{impurity}}|}, \tag{4}$$

with ϵ_0 the static dielectric constant of the medium. The small parameter leading from (1) to (2) is therefore imposed by $\varepsilon = 1/\epsilon_0$; according to [1], we shall assume that it is small enough to consider the problem as being in semiclassical regime. Hence Section 5.2 is devoted to these numerical simulations with simple initial data and a Kronig–Penney potential [36]. The Coulomb term increases the wave number of a particle close to the ionized donor's location and the WKB ansatz cannot remain single-valued because of the Γ'-periodicity of the conduction band $\kappa \mapsto E_n(\kappa)$.

For most of our examples, we checked the consistency by comparing the position densities obtained by means of the WKB approximation with the outcome of a direct simulation of the corresponding Schrödinger Eq. (2) in Section 6. However, the "independent electron" description given by (1) and (2), where interactions with other conduction electrons as well as lattice ionic cores are lumped to produce the periodic potential, is limited in at least one important direction: namely, it assumes that the electron perceives only the influence of the neighbouring ionized impurity and no repulsion from the other carriers. Hence "screening", one of the most important manifestation of e^-–e^- interaction (see [1, Chapter 17]), is completely left apart in such a simple model. A much more realistic description is given by the N-body quantum equation,

$$i\hbar\partial_t\psi_N + \frac{\hbar^2}{2m}\sum_{j=1}^{N}\partial_{x_jx_j}\psi_N = \frac{e^2}{\epsilon_0 N}\sum_{1\leqslant j<\ell\leqslant N}\frac{1}{|x_j - x_\ell|}\psi_N, \quad x \in \mathbb{R}, \tag{5}$$

with the N-wavefunction: $\psi_N \equiv \psi_N(t, x_1, x_2, \ldots, x_N)$. The Schrödinger–Poisson (Hartree) system being a mean-field approximation which has been proved to be relevant when $N \to +\infty$ (at least for bosons, i.e., without considering Pauli's exclusion principle) in [3]. WKB approximations for this weakly nonlinear model will be dealt with in the forthcoming Part 3 of this work.

2. Two-scale WKB and K-branch solutions

We are concerned with highly oscillating wave-packet solutions of the Cauchy problem for the following one-dimensional Schrödinger equation:

$$\mathrm{i}\varepsilon\partial_t\psi+\frac{\varepsilon^2}{2}\partial_{xx}\psi=\left(V\left(\frac{x}{\varepsilon}\right)+V_{\mathrm{e}}(x)\right)\psi,\qquad x\in\mathbb{R},\quad \varepsilon\to 0, \tag{6}$$

where V is 2π-periodic and V_{e} is smooth. Plane waves of the form $\psi(t,x)=A(t,x)\exp(\mathrm{i}\varphi(t,x)/\varepsilon)$ for A and φ being possibly multivalued are generally used to describe these solutions (see [9,16,33–35,46]; however this leads to a weakly coupled WKB system endowed with an Eikonal equation which still needs to be homogenized in order to describe the limiting behavior as $\varepsilon\to 0$ of (6), see e.g., [17,18,29].

2.1. Correct WKB ansatz for nonhomogeneous problems

The naive "plane wave" ansatz does not have the correct structure since it leads to a system still involving the small parameter ε. Hence following [6,15,19,30], a two-scale amplitude can be considered instead:

$$A\left(t,x,y=\frac{x}{\varepsilon}\right)=A_0(t,x,y)+\varepsilon A_1(t,x,y)+\cdots;\quad A(t,x,y+2\pi)=A(t,x,y). \tag{7}$$

We stress that in the present nonhomogeneous setting, we must assume that $A(t,x,y)\in\mathbb{C}$, (see [15]) in sharp contrast with the previously studied case for which $A(t,x,y)\in\mathbb{R}$ is sufficient. Taking this new dependence into account inside (6) yields the expression:

$$\begin{aligned}&-A\partial_t\varphi+\frac{1}{2}\left(\partial_{yy}A-A(\partial_x\varphi)^2+2\mathrm{i}(\partial_x\varphi)(\partial_yA)\right)-(V(y)+V_{\mathrm{e}}(x))A\\&\quad+\frac{\mathrm{i}\varepsilon}{2}\left(2\partial_tA+A\partial_{xx}\varphi+2\partial_xA\partial_x\varphi-2\mathrm{i}\partial_{xy}A\right)+\frac{\varepsilon^2}{2}\partial_{xx}A=0.\end{aligned} \tag{8}$$

- The O(1) terms inside (8) cancel if and only if $y\mapsto A_0(t,x,y)\exp(\mathrm{i}\kappa y)$ is an eigenstate of $\mathscr{H}(\hat{p},y)=-\frac{1}{2}\partial_{yy}+V(y)$, $\hat{p}=\mathrm{i}\partial_y$, written in Bloch wave form and associated to the eigenvalue $E(\partial_x\varphi)=-\partial_t\varphi-V_{\mathrm{e}}(x)$:

  $$\mathscr{H}(y,\hat{p})(A_0\exp(\mathrm{i}\kappa y))=-(\partial_t\varphi+V_{\mathrm{e}}(x))(A_0\exp(\mathrm{i}\kappa y)),\qquad \kappa=\partial_x\varphi.$$

  That is to say, we want $y\mapsto\Psi_\kappa(y)=\exp(\mathrm{i}\kappa y)A_0(t,x,y)$ to satisfy for all $(t,x)\in\mathbb{R}^+\times\mathbb{R}$:

  $$\forall y\in\mathbb{R},\qquad \mathscr{H}(\hat{p},y)\Psi_\kappa=-\frac{1}{2}\partial_{yy}\Psi_\kappa+V(y)\Psi_\kappa=E(\kappa)\Psi_\kappa. \tag{9}$$

  Note that the slow variable x shows up only as a parameter; thus an Hamilton–Jacobi equation has been derived from this cell problem,

  $$\partial_t\varphi+E(\partial_x\varphi)+V_{\mathrm{e}}(x)=0. \tag{10}$$

- The second step consists in writing $A_0(t,x,y)=a_0(t,x)z_\kappa(y)$ with stationary 2π-periodic orthonormal modulations: $\|z_\kappa\|_{L^2(0,2\pi)}=1$. Then following [15], the solvability condition to make $\mathrm{O}(\varepsilon)$ terms disappear (using Fredholm's alternative as in [19,30]) leads to the modified transport equation: (see [19, Remark 1])

  $$\partial_ta_0+E'(\partial_x\varphi)\partial_xa_0+\frac{a_0}{2}\partial_xE'(\partial_x\varphi)+\beta(t,x)a_0=0. \tag{11}$$

The phase-shift term is purely imaginary; $\beta(t,x) = \mathrm{i}\Im\beta(t,x)$ ($\Im$ standing for the imaginary part of a complex number). It is sometimes referred to as the *Berry phase* [7], which stems from the interaction between the periodic lattice and the slowly varying potential. It reads:

$$\beta(t,x) = V_{\mathrm{e}}'(x)\int_0^{2\pi} z_\kappa(y)\overline{\partial_\kappa z_\kappa(y)}\Big|_{\kappa=\partial_x\varphi(t,x)}\,\mathrm{d}y. \tag{12}$$

However, one can always multiply (11) by $2\bar{a}_0$ and take its real part in order to derive the more usual continuity equation for the intensity $|a_0|^2$:

$$\partial_t|a_0|^2 + \partial_x\Big(|a_0|^2E'(\partial_x\varphi)\Big) = 0, \tag{13}$$

which implies that $\int_{\mathbb{R}}|a_0(t,x)|^2\,\mathrm{d}x = \int_{\mathbb{R}}|a_0(t=0,x)|^2\,\mathrm{d}x$.

All in all, starting from the Schrödinger equation (6), one has to consider the Bloch spectral decomposition (9) producing a countable set of distorted plane waves Ψ_κ^n, $n\in\mathbb{N}$, associated to the energy bands $E_n(\kappa)$. Thus a convenient nth band ansatz reads

$$\tilde{\psi}_n^\varepsilon(t,x) = a_n(t,x)\exp\left(\frac{\mathrm{i}\varphi(t,x)}{\varepsilon}\right)z_\kappa^n(x/\varepsilon), \qquad \kappa = \partial_x\varphi(t,x), \tag{14}$$

where the unknowns evolve according to the nth band WKB system (10) and (11)

$$\partial_t\varphi + E_n(\partial_x\varphi) + V_{\mathrm{e}}(x) = 0; \qquad \partial_t\mu + \partial_x\big(E_n'(\partial_x\varphi)\mu\big) = 0, \quad \mu = |a_n|^2. \tag{15}$$

Remark 1. Eq. (11) indicates that it is now a quite involved task to reconstruct the principal amplitude a_0 inside the original WKB ansatz since the Berry's term (12) has to be computed too. However, we stress that quadratic observables can still be deduced relying on the stationary phase argument presented in [29] Section 3.2 because the phase-shift term $\exp(-\mathrm{i}\int_0^t\Im\beta(\tau,x)\,\mathrm{d}\tau)$ is slowly varying. Moreover, it is known that in some cases, one can achieve $\Im\beta\equiv 0$ by means of a smooth "gauge transform" $z_\kappa(y)\mapsto\exp(\mathrm{i}\theta(y))z_\kappa(y)$, see again [15,31] and references therein.

2.2. Derivation of the Bloch spectrum and K-branch solutions

In [29], we set up a numerical procedure to solve the Sturm–Liouville eigenvalue problem (9) relying on a spectral method. Namely, we decompose each Bloch state Ψ_κ onto the base $\exp(\mathrm{i}(n+\kappa)y)$ for $n\in\mathbb{Z}$ and $\kappa\in]-\frac{1}{2},\frac{1}{2}[$:

$$\Psi_\kappa(y) = \sum_{n\in\mathbb{Z}}\Psi_\kappa^n\exp(\mathrm{i}(n+\kappa)y), \qquad \Psi_\kappa^n = \frac{1}{2\pi}\int_0^{2\pi}\Psi_\kappa(y)\exp(-\mathrm{i}(n+\kappa)y)\,\mathrm{d}y.$$

It can be noted that $\Psi_\kappa^n = \frac{1}{2\pi}\int_0^{2\pi}z_\kappa(y)\exp(-\mathrm{i}ny)\,\mathrm{d}y$, that is, the nth Fourier coefficient of the 2π-periodic modulation. The 2π-periodic potential is treated the same way:

$$V(y) = \sum_{n\in\mathbb{Z}}\hat{V}^n\exp(\mathrm{i}ny), \qquad \hat{V}^n = \frac{1}{2\pi}\int_0^{2\pi}V(y)\exp(-\mathrm{i}ny)\,\mathrm{d}y.$$

We then study the bilinear form for all $n\in\mathbb{Z}$:

$$\langle\exp(\mathrm{i}(n+\kappa)y), -\tfrac{1}{2}\partial_{yy}\Psi_\kappa + V(y)\Psi_\kappa\rangle_{L^2(0,2\pi)} - \langle\exp(\mathrm{i}(n+\kappa)y), E(\kappa)\Psi_\kappa\rangle_{L^2(0,2\pi)}.$$

It turns out that

$$\langle \exp(\mathrm{i}(n+\kappa)y), -\tfrac{1}{2}\partial_{yy}\Psi_\kappa + V(y)\Psi_\kappa\rangle_{L^2(0,2\pi)} = \tfrac{1}{2}(n+\kappa)^2\Psi_\kappa^n + \hat{V}^{n-n'}\Psi_\kappa^{n'},$$

and we are led to seek eigenvalues and eigenvectors of the truncated matrix:

$$H_\kappa = \begin{pmatrix} \hat{V}^0 + \frac{1}{2}(\kappa - N)^2 & \hat{V}^{-1} & \cdots & \hat{V}^{-2N} \\ \hat{V}^1 & \hat{V}^0 + \frac{1}{2}(\kappa - N + 1)^2 & & \vdots \\ \vdots & & \ddots & \hat{V}^{-1} \\ \hat{V}^{2N} & \cdots & \hat{V}^1 & \hat{V}^0 + \frac{1}{2}(\kappa + N)^2 \end{pmatrix}. \tag{16}$$

To carry out this diagonalization process, we chose to use the freely available SCILAB package (http://www-rocq.inria.fr/scilab/); consult [29] Section 2.2 for some numerical results on the Bloch decomposition.

The energy bands $\kappa \mapsto E_n(\kappa)$ satisfying (9), $n = 1, 2, \ldots$ are not known analytically; however, we can exploit the smoothness and symmetry of E_n (consult [10] for precise results in 1D) by writing its Fourier series (we drop hereafter the band's subscript for clarity)

$$E(\kappa) = \frac{\hat{E}_0}{2} + \sum_{q\in\mathbb{N}^*} \hat{E}_q \cos(2\pi q\kappa), \qquad \hat{E}_q = 4\int_0^{1/2} E(\kappa)\cos(2\pi q\kappa)\,\mathrm{d}\kappa. \tag{17}$$

Since the diagonalization process for (16) furnishes automatically the Fourier coefficients of the modulations z_κ, the numerical strategy to derive the energy bands starts from the discrete set of eigenvalues of (16). We apply a discrete Fourier transform in order to deduce the coefficients $\hat{E}_q$, $q \in \mathbb{N}$ which in turn allow to compute $E(\kappa)$ in (17).

We have in mind to recover the geometric solution of (10) by means of an Eulerian numerical strategy as suggested in, e.g., [20,47]. We thus differentiate (10) with respect to the space variable in order to derive a 1D scalar balance law; its geometric solution can be obtained by working out a kinetic equation [11,32]. The idea is therefore to approximate efficiently this kinetic equation by means of a finite moment system involving a closure process. Hence following [12], we briefly recall the construction of nonnegative "multibranch solutions" of the Cauchy problem for nondegenerate balance laws with $uF'(u) \geqslant 0$,

$$\partial_t u + \partial_x F(u) + G'(x) = 0, \quad u(t=0,\cdot) = u_0, \qquad x \in \mathbb{R}, \ \ t > 0 \tag{18}$$

through a kinetic formulation. For any realizable moment vector $\vec{m} \in \mathbb{R}^K$, there exists a unique so-called *K-branch Maxwellian* distribution, solution of an entropy minimization principle. It is determined by a vector of nonnegative real numbers $\vec{u} = (u_1, \ldots, u_K)$ in decreasing order and reads

$$\mathscr{M}_{K,\vec{m}}(u_1, \ldots, u_K, \xi) = \sum_{k=1}^{K} (-1)^{k-1} H(u_k - \xi), \quad u_k > u_{k+1} \geqslant 0, \tag{19}$$

where H stands for the Heaviside function. Then, "realizable moments" are given by the following map $\vec{u} \mapsto \vec{m}(\vec{u})$

$$m_\ell(u_1, \ldots, u_K) := \frac{1}{\ell}\sum_{k=1}^{K} (-1)^{k-1}(u_k)^\ell, \quad \ell = 1, \ldots, K. \tag{20}$$

It realizes a smooth one-to-one mapping of the u_ks as long as $u_k > u_{k+1}$ for all k under consideration. We refer to [12,25,28,29] for details about K-multivalued solutions. Realizable moments (20) evolve in time according to a non-strictly hyperbolic system of balance laws,

$$\partial_t \int_{\mathbb{R}^+} \theta(\xi) f(\xi)\,\mathrm{d}\xi + \partial_x \int_{\mathbb{R}^+} F'(\xi)\theta(\xi) f(\xi)\,\mathrm{d}\xi + G'(x) \int_{\mathbb{R}^+} \theta'(\xi) f(\xi)\,\mathrm{d}\xi = 0 \tag{21}$$

for $\theta(\xi) = \xi^\ell$, $\ell = 0, 1, \ldots, K-1$. System (21) diagonalizes in Riemann's coordinates; for smooth solutions, the u_ks appearing in (19) are strong Riemann invariants and each one satisfies (18). System (21) is *strictly* hyperbolic if and only if they are all distinct; in this case, $u_k > u_{k+1}$ and the map $\vec{m}$ (20) is a diffeomorphism. K-branch entropy solutions enjoy a "finite superposition principle" as shown in [44] since they match the solutions by characteristics for K big enough:

$$\forall t > 0, \qquad \dot{X}(t) = F'(U(t, X(t))), \quad \dot{U}(t, X(t)) = -G'(X(t)). \tag{22}$$

This last property is of special interest since the WKB system (15) has to be understood as a Correspondence Principle between quantum and classical mechanics. Since the Hamilton–Jacobi equation produces a smooth but possibly multivalued solution, we interpret it relying on the preceding framework; differentiating in the space variable, we pass from (10) to an equation of the type (18) for any energy band $\kappa \mapsto E_n(\kappa)$:

$$\partial_t u + \partial_x E_n(u) + V_{\mathrm{e}}'(x) = 0; \qquad F'(\xi) = E_n'(\xi), \quad G'(x) = V_{\mathrm{e}}'(x). \tag{23}$$

From (13), we deduce that the intensities $\vec{\mu}(t,x)$ corresponding to each one of the phases $u_k(t,x)$ satisfy the continuity equation:

$$\forall k = 1, 2, \ldots, K, \qquad \partial_t \mu_k + \partial_x (E_n'(u_k)\mu_k) = 0. \tag{24}$$

We shall see in the next section how to deduce them in the general case of $V_{\mathrm{e}}'(x) \neq 0$. In certain cases, some rigorous results allow to determine the correct value of $K \in \mathbb{N}$ so as to recover the geometric solution of (23); see [29,32].

2.3. Numerical schemes for weak external potentials (no interband transitions)

In order to cope with the framework presented in Section 2.2, we plug $F'(u) = E'(u)$ in (18) and this leads us to: ($\ell = 0, \ldots, K-1$)

$$\partial_t \left(\int_{\mathbb{R}^+} \xi^\ell f(\xi)\,\mathrm{d}\xi \right) + \partial_x \left(\int_{\mathbb{R}^+} \xi^\ell E'(\xi) f(\xi)\,\mathrm{d}\xi \right) = -\ell V_e'(x) \left(\int_{\mathbb{R}^+} \xi^{\ell-1} f(\xi)\,\mathrm{d}\xi \right). \tag{25}$$

We mention that (25) constitutes a nonstrictly hyperbolic system which is furthermore nongenuinely nonlinear in the sense of Lax since the energy bands are 1-periodic. Its fluxes read therefore,

$$\int_{\mathbb{R}^+} \xi^\ell E'(\xi) f(t,x,\xi)\,\mathrm{d}\xi = \sum_{q \in \mathbb{N}^*} -\hat{E}_q \int_{\mathbb{R}^+} 2\pi q \xi^\ell \sin(2\pi q \xi) f(t,x,\xi)\,\mathrm{d}\xi,$$

where $\ell = 0, \ldots, K-1$ and $f(t,x,\xi) = \sum_{k=1}^{K} (-1)^{k-1} H(u_k(t,x) - \xi)$. The right-hand side can be computed exactly with integrations by parts, see [29]. From now on, we consider a uniform Cartesian grid determined by the two positive parameters Δx, Δt which stand for the mesh-size and the time-step, respectively. We shall denote $x_j = j\Delta x$, $x_{j+1/2} = (j+1/2)\Delta x$, $t^n = n\Delta t$, and generic computational cells read

$$T_j^n = \left[t^n, t^{n+1}\right[\times \left]x_{j-\frac{1}{2}}, x_{j+\frac{1}{2}}\right[\qquad (j,n) \in \mathbb{Z} \times \mathbb{N},$$

with the parameter $\lambda = \Delta t/\Delta x$. Then, for a given $K > 1$, the grid functions $(\vec{m}_j^n, \vec{\mu}_j^n) \in (\mathbb{R}^K)^2$ stand for some numerical approximations of the moments in (25) $\vec{m}(t^n, x_j)$ and the intensities $\vec{\mu}(t^n, x_j)$ in (24) on each T_j^n. We

recall that in the homogeneous case $V_e(x) \equiv C \in \mathbb{R}$, K-branch solutions are updated in time by means of an explicit Euler marching method:

$$\vec{m}_j^{n+1} = \vec{m}_j^n - \frac{\lambda}{2}\Big(F_K(\vec{m}_j^n, \vec{m}_{j+1}^n) - F_K(\vec{m}_{j-1}^n, \vec{m}_j^n)\Big), \qquad j \in \mathbb{Z}. \tag{26}$$

Relying on previous experience [25,27,28], we selected the simple *local Lax–Friedrichs* (LLxF for short) numerical flux which in the present setting reads:

$$F_K(\vec{m}_j^n, \vec{m}_{j+1}^n) = \left\{ \sum_{k=1}^{K} (-1)^{k-1} \left(\int_0^{(u_k^\ell)_j^n} + \int_0^{(u_k^\ell)_{j+1}^n} \right) \xi^{\ell-1} E'(\xi)\, \mathrm{d}\xi \right\}_{\ell=1,\dots,K} - \max_{k;j,j+1} |E'(u_k)|^n \Big(\vec{m}_{j+1}^n - \vec{m}_j^n\Big). \tag{27}$$

A crucial step lies clearly in finding out the relations between the moments m_ks and the Riemann coordinates u_ks; they constitute a Vandermonde system and have been solved in [44] for $K = 3, 4$ (the case $K = 2$ is simple [12]). In the general case, $K \in \mathbb{N}$, the "Markov power moment problem" (20) has been solved exactly in [45]. However, the numerical implementation of this exact solution is delicate and one could prefer the point of view of an inverse problem for the quadrature formula,

$$\int_{\mathbb{R}^+} \xi^\ell \mathscr{M}_{K,\vec{m}}(\xi)\, \mathrm{d}\xi = \frac{1}{\ell+1} \sum_{k=1}^{K} (-1)^{k-1} u_k^{\ell+1}, \qquad \ell = 0, 1, \dots, K-1,$$

as developed for instance in [21,48]. So, in this perspective the K-branch solutions u_k's are but the zeros of the Chebyshev polynomials associated to the Maxwellian distribution $\mathscr{M}_{K,\vec{m}}(\xi)$. In this work, we still assume that the number of phases will be limited in such a way the exact formulas of [44] permit to carry out the inversion of the moment map $\vec{m}$ (20). Hence the scheme is fully determined by its numerical flux (27) which can be seen as a flux-splitting method.

An additional feature to be included now is the handling of the source terms rendering for the exterior potential $V_e(x)$; the most reliable way to achieve this is to follow the well-balanced (WB) canvas. Relying on [24,25], this procedure consists in localizing in space the exterior potential; hence the right-hand side of (25) becomes

$$-\ell \Delta x \sum_{j \in \mathbb{Z}} V_e'(x) \left(\int_{\mathbb{R}^+} \xi^{\ell-1} f(t, x, \xi)\, \mathrm{d}\xi \right) \delta(x - x_{j-\frac{1}{2}}), \qquad \ell = 0, \dots, K-1,$$

where $\delta(\cdot)$ stands for the Dirac mass in $x = 0$. Then the scheme (26) is modified accordingly:

$$\vec{m}_j^{n+1} = \vec{m}_j^n - \frac{\lambda}{2}\Big(F_K(\vec{m}_j^n, \vec{m}_{j+\frac{1}{2}}^-) - F_K(\vec{m}_{j-\frac{1}{2}}^+, \vec{m}_j^n)\Big), \qquad j \in \mathbb{Z}, \tag{28}$$

where the "interface values" are given by

$$\begin{cases} \vec{m}_{j+\frac{1}{2}}^- = \vec{m}(\vec{u}_{j+\frac{1}{2}}^-), \quad E(\vec{u}_{j+\frac{1}{2}}^-) = E(\vec{u}_{j+1}^n) + V_e(x_{j+1}) - V_e(x_j), \\ \vec{m}_{j-\frac{1}{2}}^+ = \vec{m}(\vec{u}_{j-\frac{1}{2}}^+), \quad E(\vec{u}_{j-\frac{1}{2}}^+) = E(\vec{u}_{j-1}^n) + V_e(x_{j-1}) - V_e(x_j), \end{cases} \tag{29}$$

which means that one locally follows steady-state curves of (25) starting from $\vec{u}_{j\pm1}^n$. In case system (25) is at steady-state, $\vec{m}_{j+\frac{1}{2}}^- = \vec{m}_{j-\frac{1}{2}}^+ = \vec{m}_j^n$, and this implies $\vec{m}_j^{n+1} = \vec{m}_j^n$ for all $j, n \in \mathbb{Z} \times \mathbb{N}$; this is the WB property. However, since the energy bands $\kappa \mapsto E_n(\kappa)$ are not known explicitly, the computational cost of this root-finding procedure might be considered as too high. Therefore, in case $\|V_e\|_{C^2_{\mathrm{loc}}(\mathbb{R})}$ takes only moderate values, one can relax this processing combining every time-step (26) with

$$\forall j \in \mathbb{Z}, \qquad \partial_t \vec{u}(t,x_j) = V_e'(x_j), \tag{30}$$

to go back to a "Riemann coordinates" time-splitting approach. Another possibility to exploit (29) lies in using the explicit formulas of the (periodized) parabolic band approximation or the homogenized Hamiltonian when the conduction band lies completely in the classical regime (see [17,18,29]) in order to approximate the inverse of $\kappa \mapsto E(\kappa)$.

The phase-shifts (12) $\beta_k(t,x)$, $k = 1,2,\ldots,K$ that would be needed to build up the full WKB ansatz (14) read therefore:

$$\beta_k(t,x) = V_e'(x) \int_0^{2\pi} z_\kappa(y) \overline{\partial_\kappa z_\kappa(y)} \Big|_{\kappa = u_k(t,x)} \mathrm{d}y, \qquad k = 1,2,\ldots,K.$$

In order to complete the ansatz (14), we still have to deduce the values of $\vec{\mu}(t^n,x_j)$ for j,n in $\mathbb{Z} \times \mathbb{N}$ once the K-branch solutions $u_k(t^n,\cdot)$ are known at some time $t^n = n\Delta t > 0$. This will be done accordingly; for all k under consideration, we deduce from (24) that

$$\mu_k(t,x) = \mu(t=0,x_0) \left| \frac{\partial x_0}{\partial x} \right|, \qquad x = x_0 + \int_0^t E'(u_k(s,X(s)))\,\mathrm{d}s, \tag{31}$$

and this paves the way for recovering numerically the $\vec{\mu}_j^n$ out of the set of $\vec{u}_j^n$ for all $j \in \mathbb{Z}$, $k = 1,\ldots,K$. In the general case, one can always write out of the Hamiltonian system (22) and (23) that,

$$\frac{\mathrm{d}}{\mathrm{d}t} E(U) = \dot{U} E'(U) = -V_e'(X) E'(U) = -V_e'(X)\dot{X} = -\frac{\mathrm{d}}{\mathrm{d}t} V_e(X),$$

which implies the conservation of energy along characteristic curves:

$$W(X,U) := E(U) + V_e(X) = E(u_0(X(0))) + V_e(X(0)), \qquad X(0) = s.$$

So, from any abscissa $x \in \mathbb{R}$, one can trace back the characteristic curve associated to the corresponding value of $u_k(t,x)$ and each one satisfies

$$\forall k = 1,2,\ldots,K, \qquad E(u_k(t,x)) + V_e(x) = E(u_0(s^k)) + V_e(s^k). \tag{32}$$

This is a nonlinear equation for each s^k where all functions involved are smooth. In case the initial phase φ_0 is sufficiently slowly varying and V_e is monotone, the following function:

$$[0,2\pi] \ni s \mapsto \mathscr{F}(s) = W(s,u_0(s)) = E(u_0(s)) + V_e(s), \tag{33}$$

is strictly monotone thus Newton's algorithm for the equations

$$\mathscr{F}(s^k) - E(u_k(t,x)) + V_e(x) = 0, \qquad x \in [0,2\pi], \quad k = 1,2,\ldots,K, \tag{34}$$

will be efficient. For each $x_j = j\Delta x$, $j \in \mathbb{Z}$, one can obtain the K corresponding values s_j^k relying on the formula (17). Thus intensities can be obtained by means of the centered approximation:

$$\forall k = 1,2,\ldots,K, \qquad (\mu_k)_j^n = \mu(t=0,s_j^k) \left| \frac{s_{j+1}^k - s_{j-1}^k}{2\Delta x} \right|. \tag{35}$$

It can happen that for a given time $t > 0$ beyond caustic onset, $x \mapsto s_k(t,x)$ becomes discontinuous since so is $u_k(t,\cdot)$. As long as K is big enough, these points correspond to phase transitions separating for instance a monovalued region from a multivalued one. They are under-compressive shocks [28], and are located on caustics where it is anyway hopeless to expect correct values relying on the classical WKB method;

otherwise, in case K is chosen too low, compressive Lax shock appear. There are also cases for which exact computations can be achieved inside (32), see Section 3.1. We chose to limit ourselves to eight Fourier coefficients in (17) for the computations and we initialized (24) and (25) as in [29].

Remark 2. From (29) and (33), one can observe that both the well-balanced strategy for computing accurately the conservative variables $\vec{m}_j^n$ and the formula (35) to deduce the corresponding intensities $\vec{\mu}_j^n$ heavily rely on the energy conservation property; see the analogy between (32) and (29). Thus this strategy will be especially efficient on a computational level in cases where both functions $x \mapsto W(x, u_0(x))$ and $p \mapsto W(\cdot, p)$ are one-to-one; the first one in order to compute each characteristic's foot s_k, the second to derive the interface values $\vec{u}^{\pm}_{j\pm\frac{1}{2}}$ through (29). If one gives up the well-balanced option (28) and goes back to the time-splitting scheme (30), then (35) will work under a weaker condition, namely $x \mapsto \mathscr{F}(x)$ is invertible, which may restrict $\|u_0\|_{C^1}$.

Other first integrals than (32) may exist for certain problems; the MAPLE package can find them with the functions `intfactor` and `firint`.

3. Bloch oscillations; linear potential $V_e(x) = -Fx$

The theoretical work of Bloch [8], and Zener [50], has shown that semiclassical electrons within a periodic potential subject to a constant electric field F will perform temporal and spatial oscillations. These oscillations are only present if the coherence of the electron is not broken by scattering events [1]. The period (also called *Bloch time*) and total (left–right maximum) amplitude of these so-called Bloch oscillations (BO) for the full Eq. (1) are given by $\tau_B = 2\pi\hbar/eFd$ and, respectively, $L_B = \Delta/eF$ with d as the period of the potential and Δ as the width of the band in which the electrons are moving. A simple *Gedanken experiment* for realizing these oscillations in a carrier transport sense is to "put an electron" around $\kappa = 0$, switch on the field quasi-instantaneously, and monitor, e.g., the position density oscillations. This is the purpose of this section.

3.1. Setting of the problem and numerical approach

So far we are concerned with the simulation of system (25) in the special case $V_e'(x) \equiv -F$ which stands for a constant applied electric field. In this context, the WB approach outlined in Section 2.3 may be considered unnecessary; K-branch solutions are therefore to be updated by means of (26)–(30). We stress that it is possible to perform exact computations in order to extract the intensities $\mu_k(t,\cdot)$ from the velocities $u_k(t,\cdot)$ at any time $t > 0$ for $k = 1, 2, \ldots, K$. Indeed, one sees from (22) to (23):

$$\begin{cases} \frac{1}{F}\frac{\mathrm{d}}{\mathrm{d}t}E(U) = \dot{X} & \Rightarrow \quad X(t) = X(0) + \frac{1}{F}\{E(U) - E(U(0))\}, \\ \dot{U} = F & \Rightarrow \quad U = U(0) + Ft. \end{cases}$$

All in all, this leads to the analytical solution of (32),

$$\forall k = 1, 2, \ldots, K, \qquad s^k = x - \frac{1}{F}\{E(u_k(t,x)) - E(u_k(t,x) - Ft)\} \tag{36}$$

which boils down to the homogeneous formula presented in [29] as $F \to 0$ provided E is C^1. Finally, one finds an exact formula for $\vec{\mu}(t,x)$:

$$\mu_k(t,x) = \mu(t=0, s^k)\left|1 - \partial_x\left\{\frac{E(u_k(t,x)) - E(u_k(t,x) - Ft)}{F}\right\}\right|, \tag{37}$$

which can be easily approximated numerically at second order by means of centered differences: in certain situations of physical interest, this approximate formula turns out to be even exact (see Section 3.3). We found however that more accurate values for the intensities $\vec{\mu}_j^n$ can be obtained using different formulas. To this end, we explain now briefly how to generate the same solution exploiting the classical "ray-tracing method" (we shall use this technique to validate the numerical results). From (22) to (23), one deduces easily:

$$\forall s,t \in \mathbb{R}\times\mathbb{R}^+, \quad x = s + \frac{1}{F}\left(E(u_0(s)+Ft) - E(u_0(s))\right), \quad u(t,x) = u_0(s) + Ft. \tag{38}$$

Thus, intensities can be deduced the following way:

$$\mu(t,x) = \mu_0(s)\left|\frac{\partial x}{\partial s}\right|^{-1} = \mu_0(s)\left|1 + \frac{u_0'(s)}{F}\left(E'(u_0(s)+Ft) - E'(u_0(s))\right)\right|^{-1}. \tag{39}$$

It is clear that the spatial accuracy in x for the "ray-tracing method" decreases in the case rays expand, i.e., the geometrical spreading $|\frac{\partial x}{\partial s}|$ becomes big. However, formula (39) can be easily adapted to K-branch solutions $\vec{u}(t,x)$:

$$\mu(t,x) = \mu_0(s)\left|1 + \frac{u_0'(s^k)}{F}\left(E'(u_k(t,x)) - E'(u_k(t,x)-Ft)\right)\right|^{-1}. \tag{40}$$

Hence the whole ansatz (14) can be deduced from the simple numerical approach (25)–(30), supplemented by (37) or (40) as soon as the eigenstructure of the matrix (16) is known.

3.2. Superlattices and Kronig–Penney's model

The dynamics of an electron in a solid may be perturbed by, e.g., electron–phonon (crystal's vibrations) and electron–electron interactions. This is not rendered by the simple equation (1) which holds only for a perfect static lattice and carriers assumed as being independent of each other. Moreover, scattering by crystal's imperfections should be taken into account [1]; hence the Bloch time τ_B can be quite big and electrons cannot remain in ballistic regime during such a time interval. One possibility to overcome these problems is provided by *semiconductor superlattices* which consist in alternating layers of different materials (e.g., GaAs and $Al_xGa_{1-x}As$). In the simplest case, a carrier's wavefunction in the transverse direction is approximated by a plane wave for a particle of effective mass m^* [23]. In the direction perpendicular to the layers, the carrier just "sees" a juxtaposition of potential barriers, i.e., a Kronig–Penney model, see [36]. Since the period of this potential can be made several orders of magnitude larger than the original lattice's one, the Bloch time τ_B is reduced accordingly and oscillations can be monitored [38]. After an appropriate scaling, one obtains an operator of the following type:

$$V(y) = 1 - \sum_{j\in\mathbb{Z}} \mathbf{1}_{y\in[\frac{\pi}{2}+2j\pi,\frac{3\pi}{2}+2j\pi]}, \qquad \mathscr{H}_{KP}(\hat{p},x,y) = -\tfrac{1}{2}\partial_{yy} + V(y) - Fx. \tag{41}$$

and $\mathbf{1}_A$ stands for the characteristic function of a set A.

Hence we set up the discretization (26)–(37) for the initial data:

$$u_0(x) = \tfrac{1}{2}\exp\Big(-(x-\pi)^2\Big), \quad \mu_0(x) = \frac{1}{\pi}\exp\Big(-(x-\pi)^2\Big); \quad x\in[0,2\pi].$$

In Figs. 3–5 are displayed, respectively, the values of $\vec{u}(t,\cdot)$, $\vec{\mu}(t,\cdot)$ and $E'(\vec{u})(t,\cdot)$ for $t = 0.35, 0.7, 1.05, 1.4, 1.75$ (from top to bottom). The parameters were $F = 0.75$ which gives a Bloch time

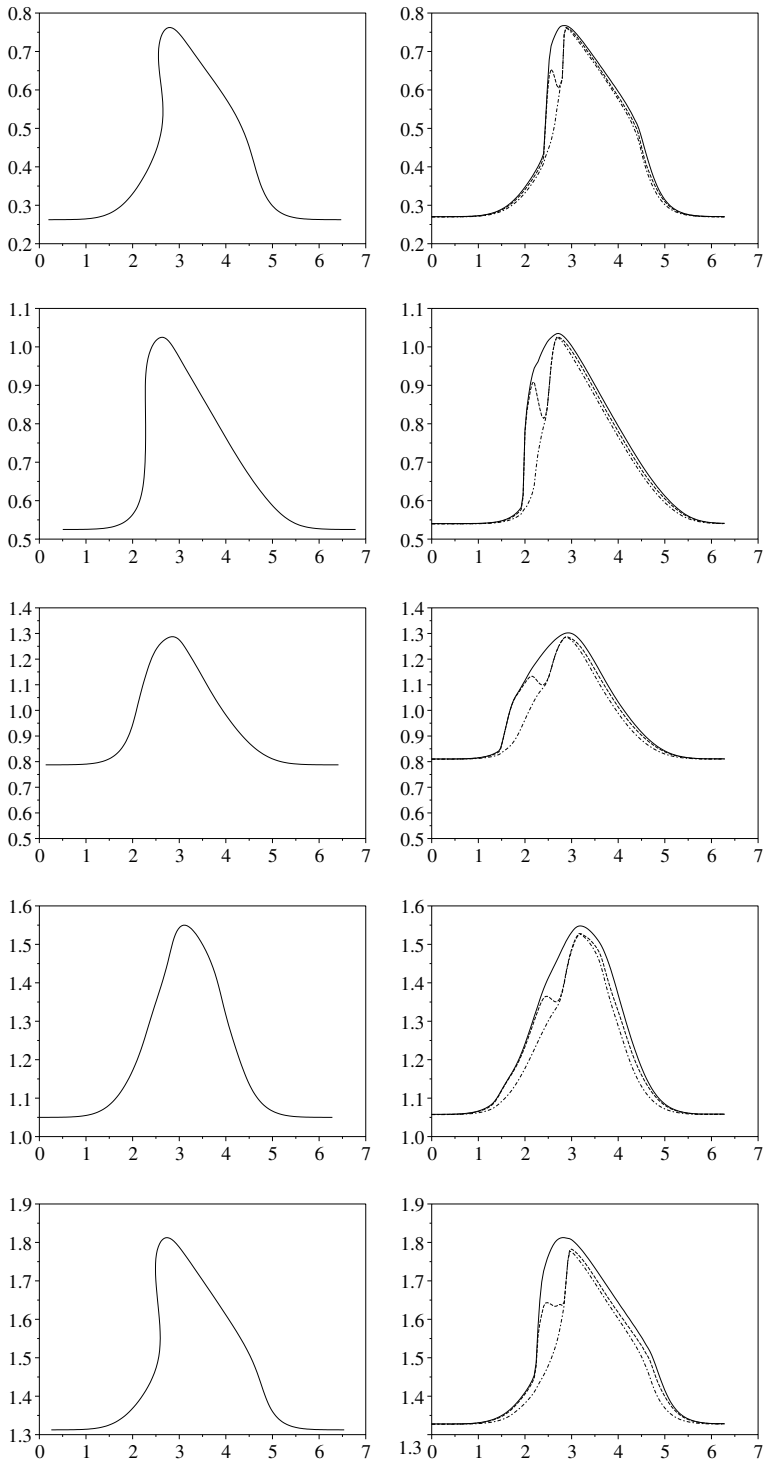

Fig. 3. Wavenumber: Ray-tracing (left), "3-branch entropy solutions" (right).

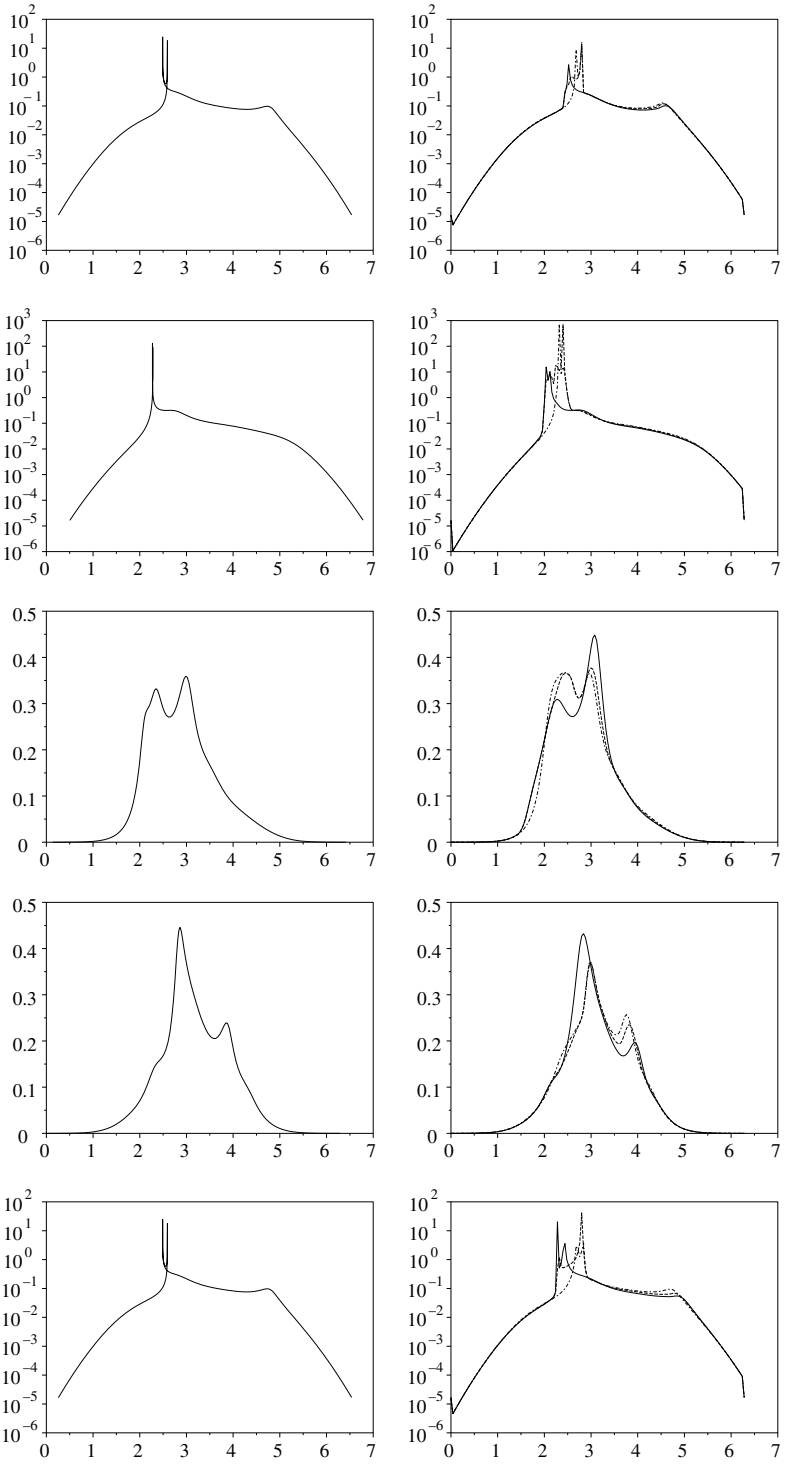

Fig. 4. Intensity: Ray-tracing (left), "3-branch entropy solutions" (right).

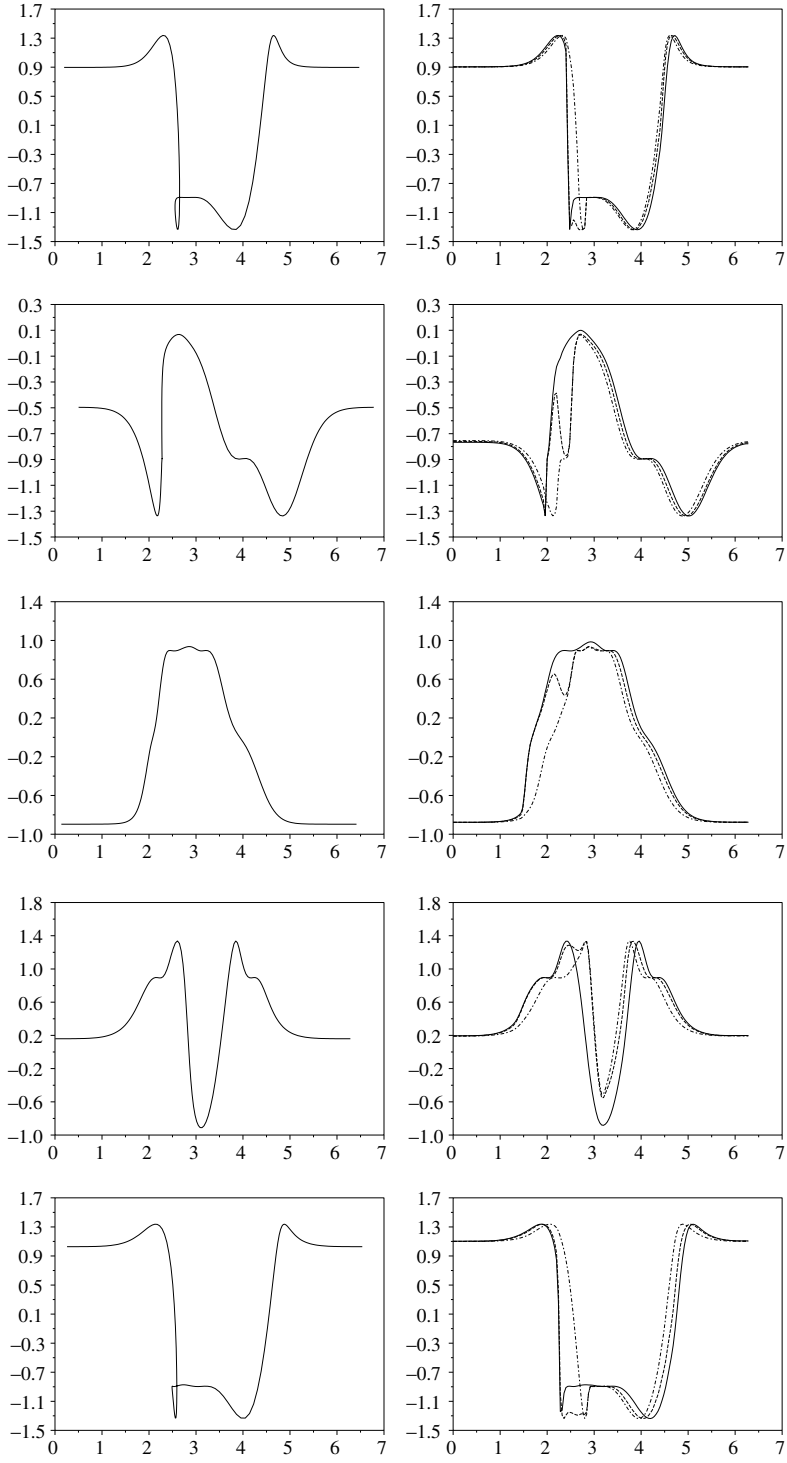

Fig. 5. Velocity $E'(\vec{u})$: Ray-tracing (left), "3-branch entropy solutions" (right).

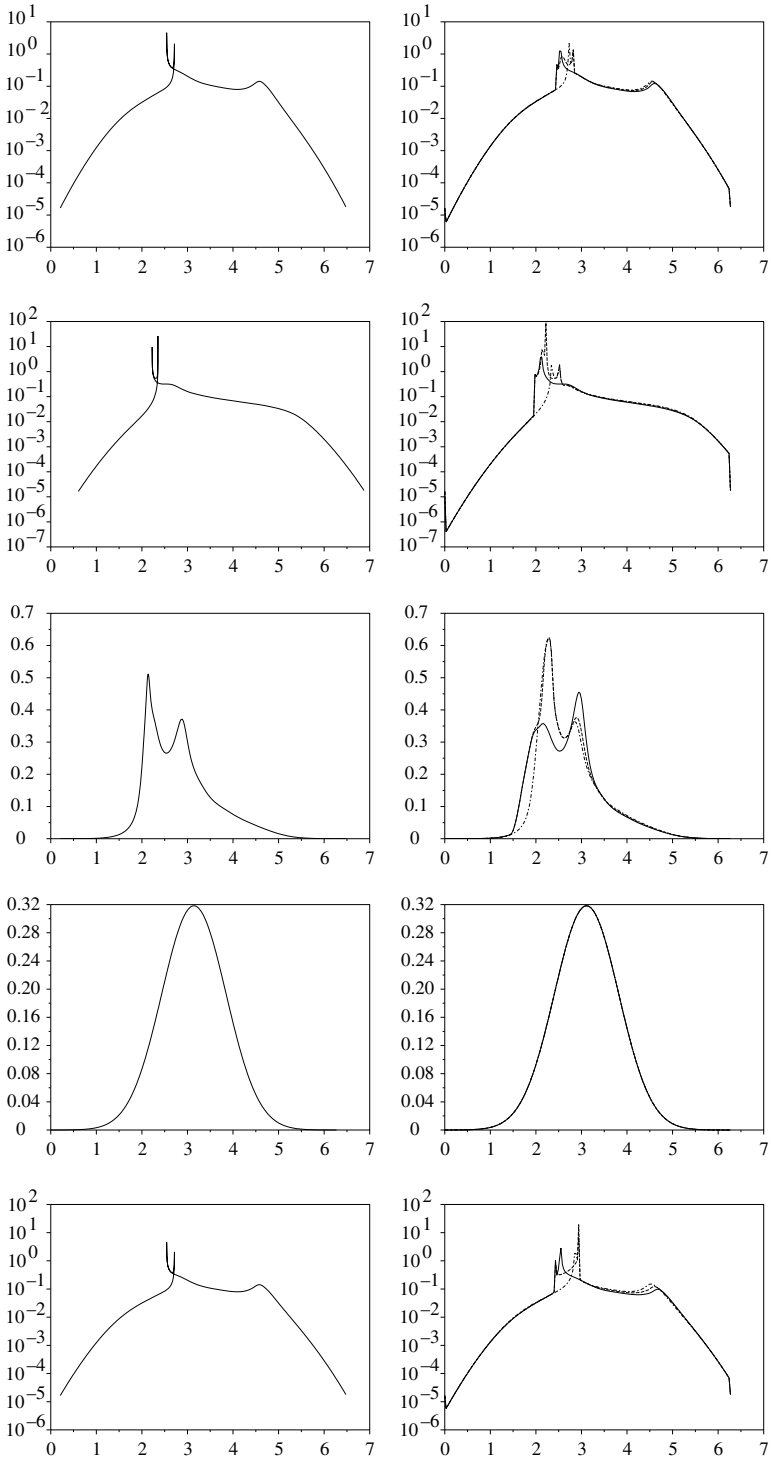

Fig. 6. Intensity: Ray-tracing (left), "3-branch entropy solutions" (right).

$\tau_B = 4/3$, $\Delta x = 0.04$ and $\Delta t = 0.03$. The periodic motion is clearly noticeable since the wavenumber $\vec{u} = \partial_x \varphi$ scans the whole Brillouin zone ($|B| = 1$). Because of the applied field, the solutions bifurcate repeatedly from one phase to three and back; this constitutes a numerical difficulty as passing from three to one phase means for the schemes turning back towards an area of nonstrict hyperbolicity in the state space.

On the one hand, it is likely that shock-capturing algorithms based on a viscous regularization of the moment Eq. (25) will not be completely satisfactory in such a situation. The numerical viscosity inherent to (26), (27) and (30) tends to separate phases even in the monovalued area as time increases; the WB approach (29) could be a possible fix in case of large time simulations, i.e., for low applied fields and big Bloch times. In particular, this explains the difference in the intensities which can be observed on the bottom of Fig. 4.

On the other hand, the "monokinetic schemes" of [27] could not lead to better results since the solution is multivalued in $T = 0.35$; hence the intensity would immediately concentrate into a Dirac measure and be further expanded with an arbitrary (unphysical) profile mainly depending on the algebra of the scheme used to solve (24). At last, we observe a good overall accuracy for the velocity $E'(\vec{u})$ throughout the whole time interval and the K-branch solutions are completely consistent with the ray-tracing algorithm.

3.3. Optical lattices and Mathieu's equation

A second experimental realization of Bloch oscillations is provided by cold atoms in optical lattices (e.g., lithium, sodium or cesium, etc.). One approximately treats them as a two-state system exposed to a strongly detuned standing laser wave which induces a force described by the potential $V(y) = \frac{\hbar\Omega_R^2}{4\delta}\cos(2k_L y)$ with $\hbar\Omega_R$ the so-called Rabi frequency, k_L the steady laser beam's wave number and δ a detuning parameter. Taking into account for gravity's force make the atoms subjects to the Wannier–Stark Hamiltonian which is smooth and reads after scaling (see [5,23,42,49]):

$$\mathscr{H}_{WS}(\hat{p}, x, y) = -\tfrac{1}{2}\partial_{yy} + \cos(y) - Fx.$$

Here, we used the discretization (26)–(37) with $F = 0.5$ for identical initial data:

$$u_0(x) = \frac{1}{2}\exp\Big(-(x-\pi)^2\Big), \quad \mu_0(x) = \frac{1}{\pi}\exp\Big(-(x-\pi)^2\Big); \quad x \in [0, 2\pi].$$

In Fig. 6, the values of $\vec{\mu}(t,\cdot)$ for $t = 0.5, 1, 1.5, 2, 2.5$ (from top to bottom) are displayed; the values of $\vec{u}(t,\cdot)$ and $E(\vec{u})(t,\cdot)$ being very similar to the ones shown in Figs. 3 and 5. The parameters used were $F = 0.5$ ($\tau_B = 2$) and $\Delta x = \Delta t = 0.03$. Since the conduction band for $V(y) = \cos(y)$ has a less steep κ-derivative, the effects of numerical viscosity are less important and phases stick more altogether. Looking at the fourth picture on the right in Fig. 6, one sees a perfect recovery of the intensity at time $T = 2$; this illustrates a situation in which the second order approximation of (37),

$$\mu_k(t, x_j) \simeq \mu_0(s^k)\left|1 - \left\{\frac{E(u_k)_{j+1} - E(u_k - Ft)_{j+1} - E(u_k)_{j-1} + E(u_k - Ft)_{j-1}}{2F\Delta x}\right\}\right|, \tag{42}$$

becomes exact even if the K-branch solutions $\vec{u}_j^n$ are not perfectly rendered. This is a consequence of the accuracy in the computation of the energy bands, see [29] and Section 2.2. If $t \div \tau_B$ the Bloch period belongs to $\mathbb{N}$, then $Ft \in \mathbb{N}$ and since the function $\kappa \mapsto E(\kappa)$ is 1-periodic, (see Section 2.1 and [29])

$$\forall u_k \in \mathbb{R}, \quad k = 1, \ldots, K, \qquad E(u_k) = E(u_k - F\tau_B).$$

Hence, the numerator of (42) is zero and $\mu_k(t, x_j) = \mu_0(x_j)$ since $y_k = x_j$ for all $k = 1, 2, \ldots, K$ is the unique solution of (36). Similarly one would establish the same property for the approximation based on (40),

$$\mu_k(t,x_j) \simeq \mu_0(s^k)\left|1+\frac{u_0'(s^k)}{F}\left(E'(u_k)_j - E'(u_k - Ft)_j\right)\right|^{-1}, \tag{43}$$

since the derivative $\kappa \mapsto E'(\kappa)$ is also 1-periodic. Thus we have proved:

Proposition 1. *For any value of $F \in \mathbb{R}^+$ in the Wannier–Stark Hamiltonian $\mathscr{H}_{WS}(\hat{p},x,y) = -\frac{1}{2}\partial_{yy} + V(y) - Fx$ with $V(y+2\pi) = V(y)$, the intensities $\vec{\mu}_j^n$ computed out of the numerical K-branch solutions $\vec{u}_j^n$, (35) and (36) with either (42) or (43) are* **exact** *at every time $T = n\tau_B$ with $n \in \mathbb{N}$ and $\tau_B = 1/F$.*

The main difference between formulas (43) and (42) is the numerical rendering of caustics. Since caustics are perceived as phase transitions for the K-branch solutions $\vec{u}_j^n$, the divided differences in (42) tend to infinity. Similar blowup would occur in (43), but for a smaller value of Δx because it does not involve any discrete differentiation. Both formulas tend to agree as Δx is decreased.

4. Study of the confining potential $V_e(x) = \frac{1}{2}x^2$

The main motivation for the study of this potential stems from optical lattices placed inside a confining magnetic field [15]; the corresponding Hamiltonian reads $\mathscr{H}_{osc}(\hat{p},x,y) = -\frac{1}{2}\partial_{yy} + \cos(y) + \frac{1}{2}x^2$. This is typically encountered while simulating, e.g., Bose–Einstein condensates submitted to a laser light, but we shall not restrict ourselves to this particular physical situation and keep on considering a generic particle submitted to both oscillating and quadratic potentials through (6).

4.1. The parabolic band approximation

We first place ourselves under the restriction of a moderate initial velocity in order to use the so-called "parabolic band approximation", see [29,43] in the present context, which consists in considering the nth energy band as given by a parabola parametrized by the effective mass:

$$E_n(\kappa) \simeq E_n(0) + \frac{\kappa^2}{2m^*}, \qquad m^* > 0.$$

In case the periodic potential in (6) is $V(x) = \cos(x)$, we found the parameters $E_3(0) = 0.8536$ and $m^* = 0.2783$. Then again, it is possible to solve the differential system of characteristics; indeed, from (22) and (23), one derives

$$\begin{pmatrix}\dot{X}\\ \dot{U}\end{pmatrix} = \begin{pmatrix}0 & \frac{1}{m^*}\\ -1 & 0\end{pmatrix}\begin{pmatrix}X\\ U\end{pmatrix}, \qquad X(0) = X_0, \quad U(0) = u_0(X_0).$$

The corresponding spectrum is $\Lambda = \{\pm i/\sqrt{m^*}\}$ and this yields a rotation in phase space:

$$\begin{cases} X(t) = \cos(t/\sqrt{m^*})X_0 + \sin(t/\sqrt{m^*})u_0(X_0)/\sqrt{m^*},\\ U(t,X(t)) = -\sqrt{m^*}\sin(t/\sqrt{m^*})X_0 + \cos(t/\sqrt{m^*})u_0(X_0).\end{cases}$$

Under the assumption of validity for this band approximation, one may use WB routines:

$$\forall j \in \mathbb{Z}, \quad \begin{cases} \vec{u}^-_{j+\frac{1}{2}} = \operatorname{sign}(\vec{u}^-_{j+\frac{1}{2}})\sqrt{(\vec{u}_{j+1})^2 + m^*(x_{j+1}^2 - x_j^2)},\\ \vec{u}^+_{j-\frac{1}{2}} = \operatorname{sign}(\vec{u}^+_{j-\frac{1}{2}})\sqrt{(\vec{u}_{j-1})^2 + m^*(x_{j-1}^2 - x_j^2)}.\end{cases}$$

Thus, following (29), one deduces the "interface moments" $\vec{m}^{\pm}_{j+\frac{1}{2}}$ to be inserted inside (28) in order to propagate K-branch solutions as times increase. As a byproduct, one is actually able to recover accurately the intensities relying on (31); more precisely,

$$\begin{cases} \mu(t,X) = \mu_0(X_0)\left|\frac{\partial X}{\partial X_0}\right|^{-1} = \mu_0(X_0)\left|\cos(t/\sqrt{m^*}) + \sin(t/\sqrt{m^*})u_0'(X_0)\right|^{-1}, \\ X_0 = \cos(t/\sqrt{m^*})X - \sin(t/\sqrt{m^*})U(t,X)/\sqrt{m^*}. \end{cases}$$

We set up the following initial data in order to carry out a numerical test on $x \in [0, 2\pi]$:

$$V_e(x) = \frac{(x-\pi)^2}{2}, \qquad u_0(x) = 0.3\sin(x), \qquad \mu_0(x) = \exp\Big(-(x-\pi)^2\Big),$$

and the results for $\Delta x = 2\pi/512$ and $t = 0.7$ are displayed on Fig. 7 where an exact ray-tracing solution is shown for comparison, see also the results in [28,33,34]. It can be noticed that the smearing of the phase boundaries on the 3-branch solutions causes two artificial spikes around $x = 3$ and $x = 3.4$ on the corresponding intensities.

4.2. Computation in the entire Brillouin zone

Looking at Fig. 7, one sees that the crystal momentum $\vec{u}(t,\cdot)$ went far beyond the limits of the Brillouin zone $B = [-\frac{1}{2}, \frac{1}{2}]$ on both sides of the domain; so the parabolic band approximation is not justified at all in this case and the correct expression (17) has to be used instead. A drawback is that the differential system

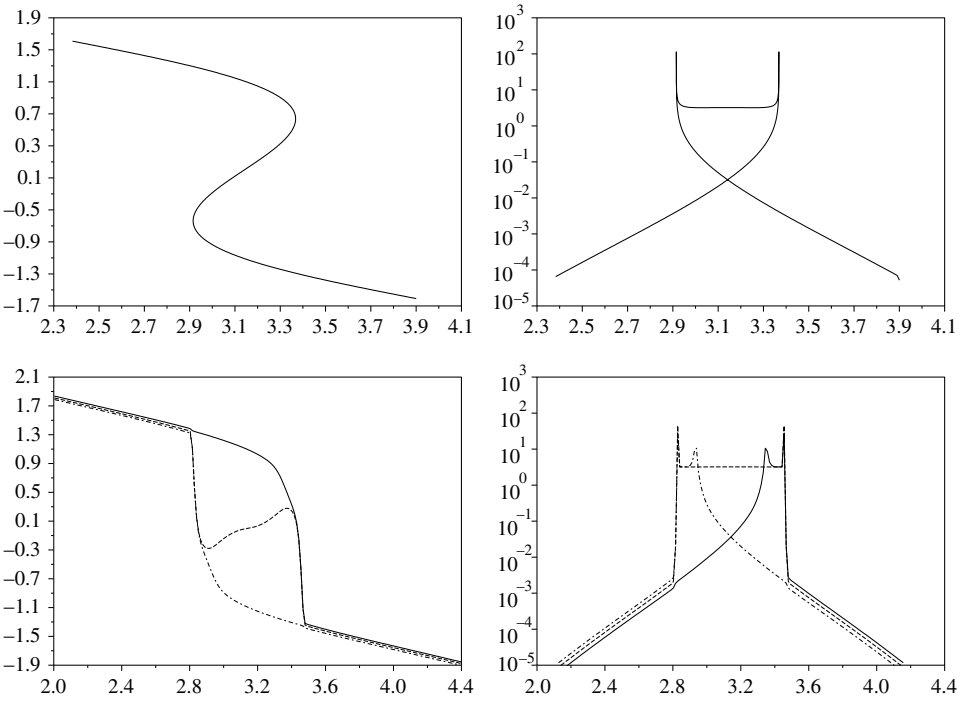

Fig. 7. "3-branch solutions" $\vec{u}$, $\vec{\mu}$ in $T = 0.7$ (bottom) and ray-tracing solution (top).

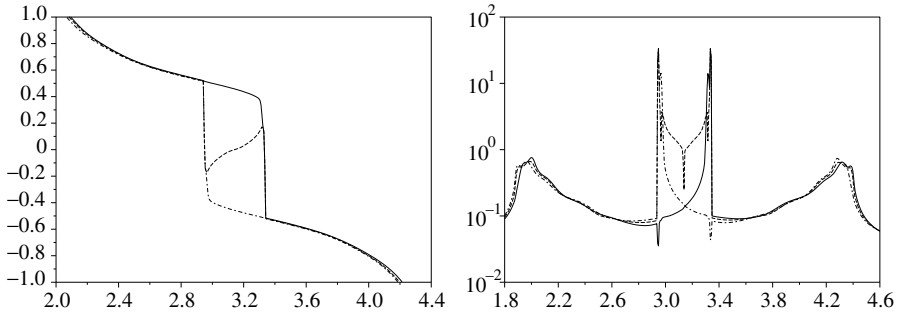

Fig. 8. "3-branch solutions" $\vec{u}$, $\vec{\mu}$ in $T = 0.85$ for the full band system.

(22) and (23) cannot be solved explicitly any more. Moreover, the Eqs. (28) and (29) become more delicate to handle. So one may choose to rely on the time-splitting approach (30).

Another consequence is that the use of the formula (35) involving discrete differentiation cannot be avoided in order to deduce intensities. However, in the present situation, the function $\mathscr{F}$ (34) is not monotone; so in the regions where two roots s^k are available for some $(t^n, x_j, \vec{u}_j^n)$, we shall always select the value minimizing the discontinuities. Hence it is interesting to set up this scheme with the preceding initial data to evaluate the reliability of both the parabolic band approximation and formula (35) to deduce intensities. The results $\Delta x = 2\pi/1024$ and $t = 0.85$ are displayed on Fig. 8. For a validation, we shall compare this approximation with a direct simulation of Schrödinger equation (6) later in Section 6.3.

5. Interaction with hydrogenic impurities; harmonic potential

On of the most important properties of semiconducting materials is that both the type and the quantity of charge carriers can be controlled through a process called *doping*. For instance, if a small quantity of Arsenic (with 5 valence electrons) is added to molten Germanium (with only 4), these impurities will crystallize into a diamond-like structure [1]. Four of the Arsenic valence electrons will participate in forming the energy bands, and the fifth one can be considered essentially free. At $T = 0$ temperature, its energy levels satisfy the "hydrogenic Hamiltonian" (3) and usually lie inside the gap below the conduction band. Hence much less energy is needed in order to make it reach the conduction band compared to the one which would be necessary for the valence electrons to trigger interband transition. Thus such an alloy contains negative charge carriers in its conduction band and is known as an *n-type semiconductor*. These impurities are hydrogenic donor atoms.

5.1. The Kronig–Penney model for materials with impurities

We can model this situation in a schematic way relying on the elementary Kronig–Penney model by making one of its wells a bit deeper than the others, just imagining that this one contains two electrons instead of one (the opposite "p-type" case, for instance, when Gallium with valence 3 is added to Germanium, is modelled in a similar way with a well a bit higher than the others and would not be considered any further). This allows for explicit computations whereas Coulomb term inside the hydrogenic Hamiltonian (3) does not.

To be more precise, we begin by approximating the differential term in (3) by means of the effective mass theory in order to get a more tractable problem,

$$\frac{1}{2m^*}\partial_{yy}\Psi(y) + (E - V(y))\Psi = 0, \qquad V(y) = 1 - 2\mathbf{1}_{|y|\leqslant\pi}. \tag{44}$$

This differential equation splits into two thanks to the form of V,

$$\frac{1}{2m^*}\partial_{yy}\Psi_1(y) + (E+1)\Psi_1 = 0, \qquad \frac{1}{2m^*}\partial_{yy}\Psi_2(y) + (E-1)\Psi_2 = 0,$$

coupled by boundary conditions in $\pm\pi$:

$$\Psi_1(\pm\pi) = \Psi_2(\pm\pi), \qquad \partial_y\Psi_1(\pm\pi) = \partial_y\Psi_2(\pm\pi).$$

A base of solutions is $\exp(\pm\kappa_1 y)$ and $\exp(\pm\kappa_2 y)$ with $\kappa_1 = \sqrt{2m^*(1-E)}$ and $\kappa_2 = i\sqrt{2m^*(1+E)}$. The C^1 regularity requirement in $y = \pm\pi$ implies that,

$$\kappa_2 = \kappa_1 \tan(\pi\kappa_1), \qquad \kappa_2 = \kappa_1 \operatorname{cotan}(\pi\kappa_1),$$

together with:

$$(\kappa_1)^2 + (\kappa_2)^2 = 4m^*.$$

This set of algebraic equations can be solved and results for $m^* = 0.2$ are shown in Fig. 9. There are three bound states associated to (44), one of them being located just below the conduction band.

5.2. Numerical simulation of the Coulomb interaction

We consider the Kronig–Penney's potential as in (41) and we set up the "3-branch systems" (25) with the Coulomb term reading

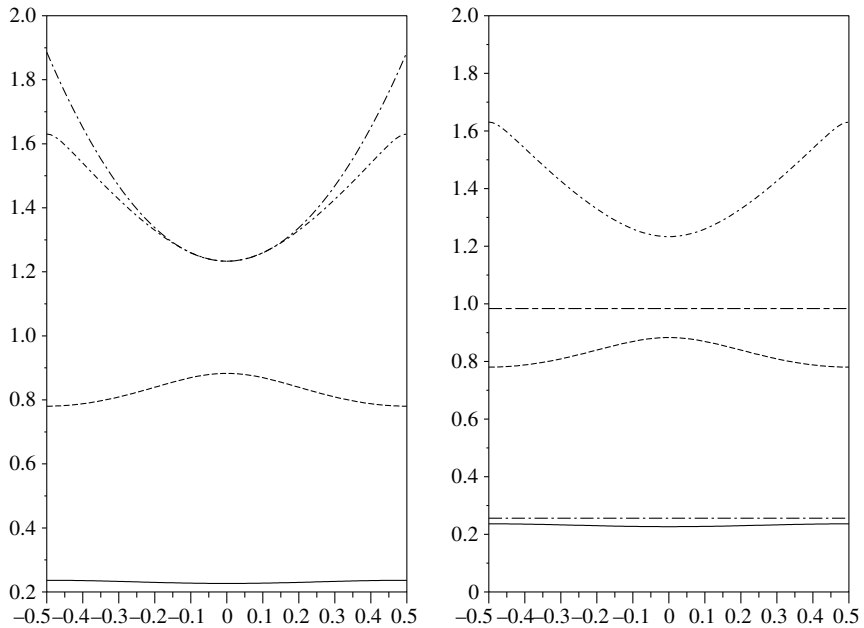

Fig. 9. Lowest energy bands and parabolic approximation for Kronig–Penney's model (left), with two hydrogenic levels superimposed (right).

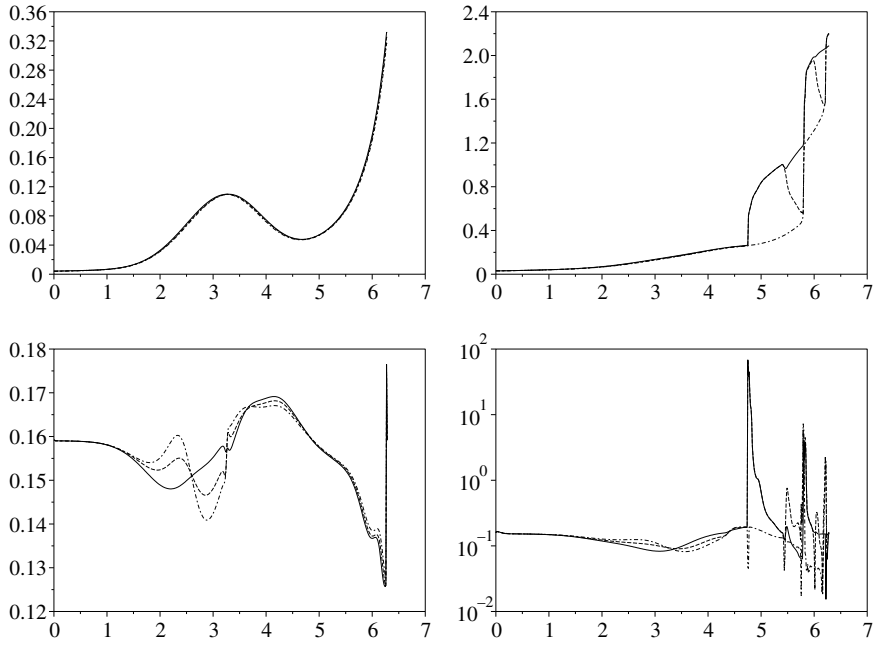

Fig. 10. "3-branch solutions" $\vec{u}$ and $\vec{\mu}$ in $T = 0.2$ (left) and $T = 1.5$ (right).

$$V_e(x) = -\frac{1}{|x-7|}, \qquad x \in [0, 2\pi],$$

which means that the ionized impurity stands a bit outside of the right border of the computational domain. This allows to prevent numerical overflow issues during computations (another possibility could have been to truncate it). Numerical simulations are carried out relying on (26)–(30) with initial data:

$$u_0(x) = \frac{3}{10\pi}\exp(-(x-\pi)^2), \qquad \mu_0(x) = \frac{1}{2\pi}. \tag{45}$$

We chose $\Delta x = 2\pi/512$, $\Delta t = 2\Delta x/3$ and computed the quantities appearing in the WKB ansatz in both $T = 0.2$ (single-valued solution) and $T = 1.5$ (two cusps have developed); see Fig. 10. One can observe that the attractive Coulomb term increases the "crystal momentum" in a close neighbourhood of the impurity location. Because of the periodicity of $\kappa \mapsto E(\kappa)$, this makes the particle oscillate inside this region and multivaluations develop. The corresponding intensities have been computed by means of (35) after solving (34) for all $x_j \in [0, 2\pi]$ since for our data (45), (33) is strictly decreasing. We shall come back to this case in Section 6.2.

6. Comparisons with direct Schrödinger simulations

In order to check consistency with the genuine Schrödinger equation, we simulated some variants of (2) with initial data corresponding to (14) by means of a Fourier solver in order to compare the resulting position densities. We have in mind to extend the consistency results of [26]. For simplicity in the presentation, we worked with Mathieu's potential $V(x) = \cos(x)$; however, results would be similar for Kronig–Penney's model.

6.1. Homogeneous case: post-breakup consistency

As we believe it is an important question whether or not the present WKB strategy can permit to recover reliable approximations of quadratic observables in the small ε regime, let us come back first to the numerical tests already carried out in [29], namely:

- a set of initial data which permit to compute within the so-called "parabolic band approximation":

$$u_0(x) = 0.3\sin(x), \qquad \mu_0(x) = \exp\Big(-(x-\pi)^2\Big), \tag{46}$$

- another one which takes place inside the full Brillouin zone $[-\frac{1}{2},\frac{1}{2}]$:

$$u_0(x) = \frac{1}{2}\exp\Big(-(x-\pi)^2\Big), \qquad \mu_0(x) = \frac{1}{\pi}\exp\Big(-(x-\pi)^2\Big). \tag{47}$$

As both ray-tracing and K-branch solutions have been displayed in [29], we want here to concentrate more on the consistency with a direct Schrödinger computation carried out relying on the time-splitting spectral schemes presented in [2]. We recall now briefly the numerical Fourier solver they set up for solving (2) with $V(x) = \cos(x)$ and some exterior potential $V_e(x)$. One sets up the ansatz (14) which reads (we dropped the nth band index for clarity):

$$\psi^\varepsilon(t=0,x) = \sqrt{\mu_0(x)}\exp(\mathrm{i}\varphi_0(x)/\varepsilon) z_{u_0(x)}(x/\varepsilon). \tag{48}$$

Then, the corresponding solution $\psi^\varepsilon(t,\cdot)$ is expanded in its Fourier series for $x \in [0,2\pi]$:

$$\psi^\varepsilon(t,x) = \sum_{q\in\mathbb{Z}} \hat{\psi}_q^\varepsilon(t)\exp(\mathrm{i}qx), \qquad \hat{\psi}_q^\varepsilon(t) = \frac{1}{2\pi}\int_0^{2\pi} \psi^\varepsilon(t,x)\exp(-\mathrm{i}qx)\,\mathrm{d}x,$$

and a time-step $\Delta t > 0$ being given, one solves iteratively the free Schrödinger equation by means of an explicit Fourier scheme,

$$i\varepsilon\partial_t\psi^\varepsilon + \frac{\varepsilon^2}{2}\partial_{xx}\psi^\varepsilon = 0 \iff \hat{\psi}_q^\varepsilon(t) = \exp\big(-\mathrm{i}\varepsilon(t-t')q^2/2\big)\hat{\psi}_q^\varepsilon(t'), \qquad t > t' \geqslant 0,$$

for $q \in \mathbb{Z}$, and then the differential equation associated with both potentials:

$$\mathrm{i}\varepsilon\partial_t\psi^\varepsilon = \Big(V\Big(\frac{x}{\varepsilon}\Big) + V_e(x)\Big)\psi^\varepsilon \iff \psi^\varepsilon(t,x) = \exp\big(-\mathrm{i}(t-t')[V(x/\varepsilon) + V_e(x)]/\varepsilon\big)\psi^\varepsilon(t',x).$$

We refer to [2] for more details. Since this approach needs to use repeatedly the `fft` algorithm, we used only vectors which length is a power of 2 in order to maximize the efficiency. Concerning the WKB approximation, according to [29] Section 3.2, its "3-branch position density" $\rho^\varepsilon_{\mathrm{WKB}}(t,x)$ is meant to be:

$$\rho^\varepsilon_{\mathrm{WKB}}(t,x) = \begin{cases} \mu_2(t,x)|z^n_{u_2(t,x)}(x/\varepsilon)|^2 & \text{if } |s^1 - s^3|(t,x) \leqslant \alpha\Delta x, \\ \sum_{k=1}^3 \mu_k(t,x)|z^n_{u_k(t,x)}(x/\varepsilon)|^2 & \text{otherwise.} \end{cases} \tag{49}$$

Of course, the $s^k(t,x)$ aforementioned are the roots of the equation (34) solved at any time t for all $x \in [0,2\pi]$. We selected $\Delta t = 0.01$ independent of ε and $\alpha = 5$. Comparing the position densities for initial data (46) gives the outcome displayed on Fig. 11. Following [13], we tried to check on the right column a weak convergence as $\varepsilon \to 0$ by looking at the antiderivative of the difference of the densities; thus we shall study the function

$$x \mapsto \int_0^x \Big(\rho^\varepsilon_{\mathrm{WKB}}(T,s) - |\psi^\varepsilon(T,s)|^2\Big)\,\mathrm{d}s, \tag{50}$$

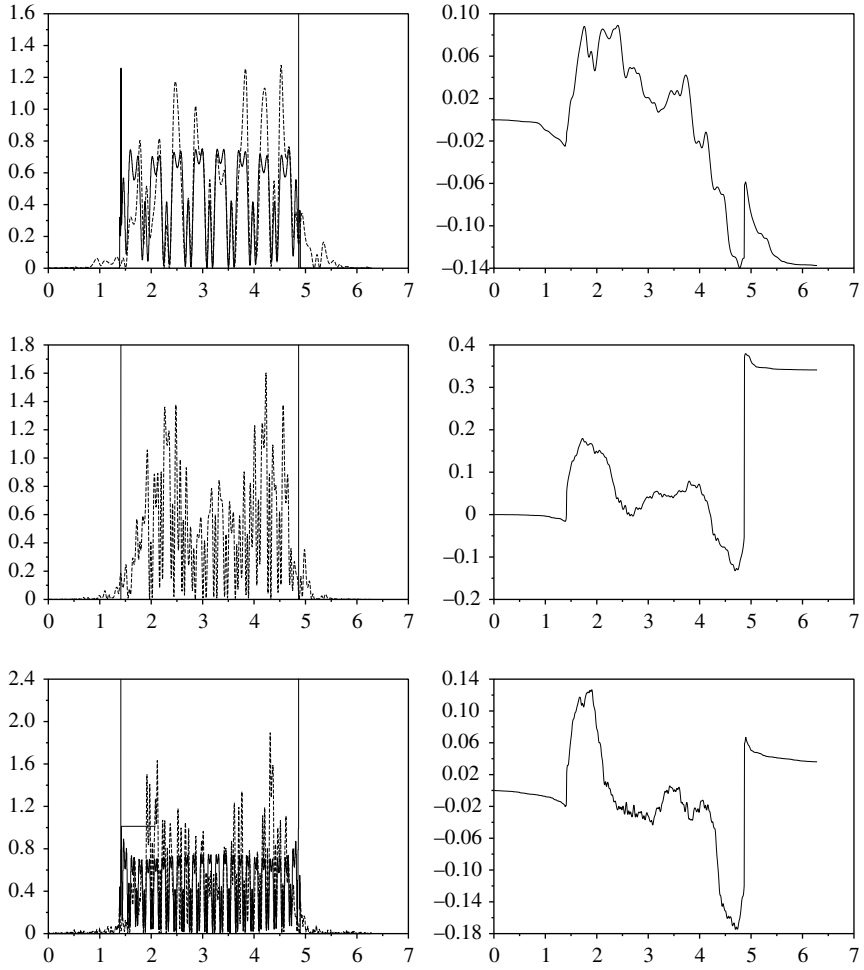

Fig. 11. Comparison $\rho^{\varepsilon}_{\mathrm{WKB}}$ (solid) vs. $|\psi^{\varepsilon}|^2$ (dotted) (left) and weak consistency (50) (right) in $T = 3$ for $\varepsilon = 1/15, 1/30, 1/42$ (top to bottom) with Mathieu's potential.

which can be expected to flatten as ε is decreased. Lemma 2.1 in [13] ensures that the L^1 norm of (50) going to zero is equivalent to the weak convergence of $\rho^{\varepsilon}_{\mathrm{WKB}}$. On Fig. 12, we display the evolution of both $\rho^{\varepsilon}_{\mathrm{WKB}} - |\psi^{\varepsilon}|^2$ and (50) in the $L^1(\mathbb{R})$ norm; only weak convergence seems to be possibly hoped for, as could have been expected, [10,22,39]. One can explain the strongly "non-monotonic" decay of Fig. 12 as follows: the biggest source of error is generally located on the caustic curve, so according to the value of the modulations $|z^n_{u_k(t,x)}(x/\varepsilon)|^2$ at these points, the L^1 norm of (50) can change notingly.

The comparison of position densities for the initial data (47) leads to the results shown on Fig. 13. Since the crystal momentum is bigger, more caustics developed and the outcome is more complex; see [29] Fig. 9 for a ray-tracing picture. We also tried to check weak convergence of the densities numerically through the function (50) becoming flat on Fig. 13. Despite the fact we could not obtain a clear picture like Fig. 12 we notice that the interval of variation is smaller for $\varepsilon = 1/30$ than for $\varepsilon = 1/15$. After breakup, the Fourier scheme can be completely overwhelmed for too small values of εM; in such a case, the quadratic observables are simply wrong as explained in, e.g., [2,40]. We tried to avoid this phenomenon by using a high number of coefficients inside our Fourier schemes: Figs. 11 and 13 have been obtained with 4096 coefficients.

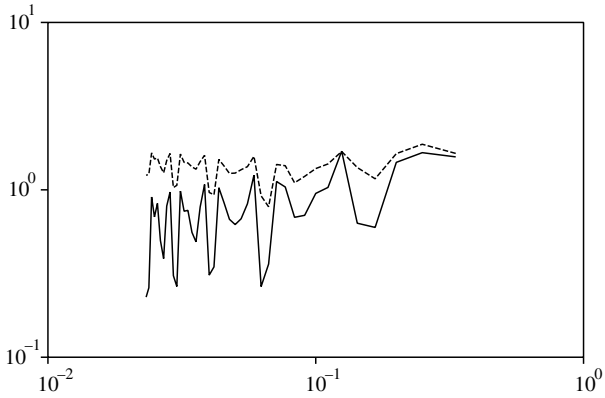

Fig. 12. Decay of $\|\rho^{\varepsilon}_{\mathrm{WKB}}(T,\cdot) - |\psi^{\varepsilon}|^2(T,\cdot)\|_{L^1}$ (dotted) and L^1 norm of the function (50) (solid) for $T = 3$ with respect to ε.

The general aspect of the position density looks like being stable for reasonably small values of ε. This suggests that both the WKB ansatz (15) and the "3-branch density" (49) could be valid for (6) with $V_e(x) \equiv 0$ in the semiclassical regime. The next subsections are devoted to the nonhomogeneous case $V_e(x) \neq 0$.

6.2. Nonhomogeneous case: the Coulomb potential

We are again concerned with the case where (6) is endowed with the Coulomb interaction term as in Section 5.2 with identical initial data (45):

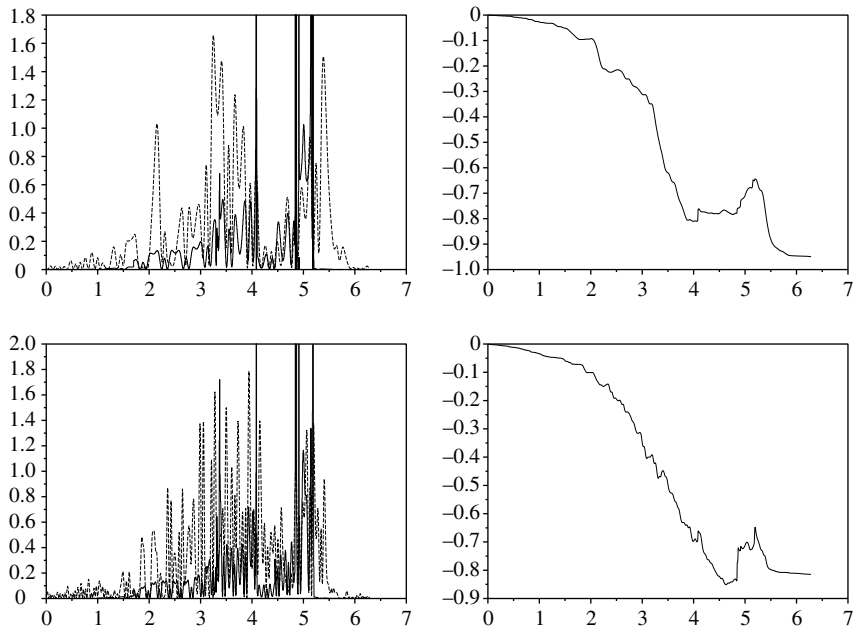

Fig. 13. Comparison $\rho^{\varepsilon}_{\mathrm{WKB}}$ (solid) vs. $|\psi^{\varepsilon}|^2$ (dotted) (left) and weak consistency (50) (right) in $T = 1.5$ for $\varepsilon = 1/15, 1/30$ (top to bottom) with Mathieu's potential.

$$V_{\mathrm{e}}(x) = -\frac{1}{|x-7|}, \qquad \hat{V}_{\mathrm{e}}^{\ell} = \frac{1}{2\pi}\int_0^{2\pi} V_{\mathrm{e}}(x)\exp(-\mathrm{i}\ell x)\,\mathrm{d}x.$$

As explained in [29], Section 5.3, for all $t > 0$, the Fourier coefficients $\hat{\psi}_q(t)$ satisfy the following differential system because for the Mathieu's equation, we have $V(x) = \frac{\exp(\mathrm{i}x)+\exp(-\mathrm{i}x)}{2}$:

$$\forall q \in \mathbb{Z}, \quad \mathrm{i}\varepsilon\frac{\mathrm{d}}{\mathrm{d}t}\hat{\psi}_q^{\varepsilon}(t) = \frac{1}{2}\left(\hat{\psi}_{q-\frac{1}{\varepsilon}}^{\varepsilon}(t) + q^2\varepsilon^2\hat{\psi}_q^{\varepsilon}(t) + \hat{\psi}_{q+\frac{1}{\varepsilon}}^{\varepsilon}(t)\right) + \sum_{\ell\in\mathbb{Z}} \hat{V}_{\mathrm{e}}^{\ell}\hat{\psi}_{q-\ell}^{\varepsilon}(t), \tag{51}$$

where $\hat{V}_{\mathrm{e}}^{\ell}$ stand for the Fourier coefficients of the exterior potential. This differential equation can be integrated as soon as the coefficients $(V_{\mathrm{e}}^{\ell})_{\ell\in\mathbb{Z}}$ are known. However, such a numerical approach is limited because of the matrix exponential `expm` function, whose accuracy decreases with the number of Fourier modes involved and in practice does not allow to go beyond 512 modes. Hence we shall again rely on the time-split Fourier schemes advocated in [2] in order to carry out reliable Schrödinger simulations. We chosed to work again with 4096 modes whereas the density corresponding to the WKB ansatz has been

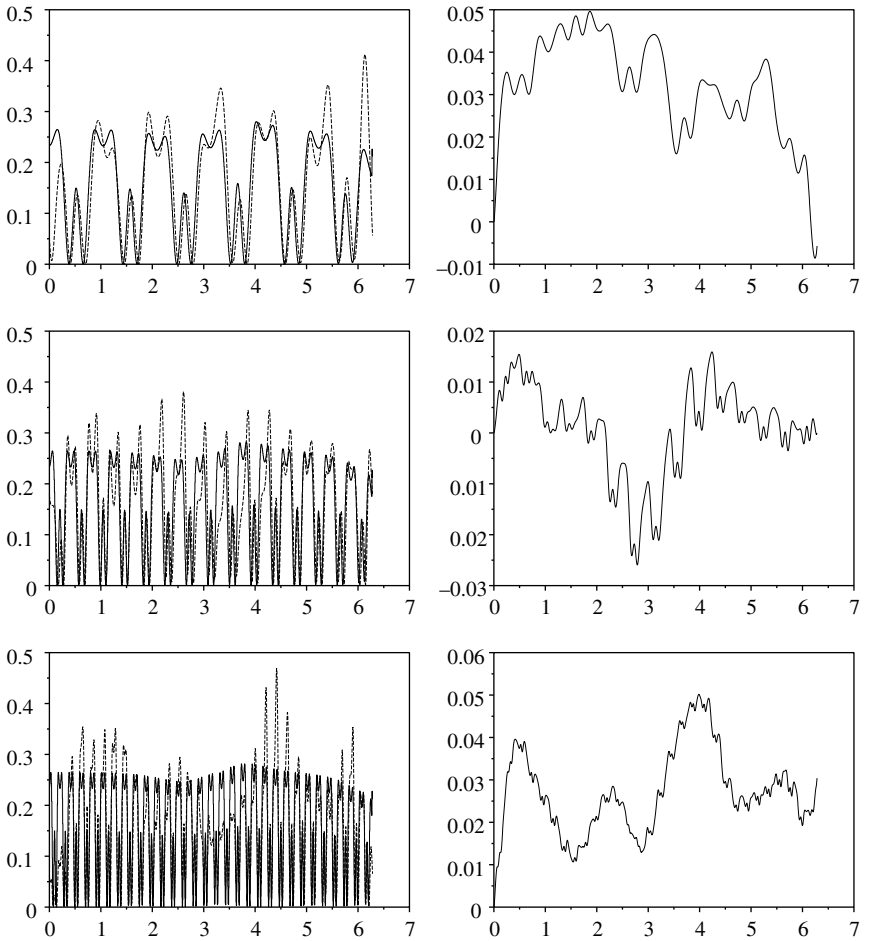

Fig. 14. Comparison $\rho_{\mathrm{WKB}}^{\varepsilon}$ (solid) vs. $|\psi^{\varepsilon}|^2$ (dotted) (left) and weak consistency (50) (right) in $T = 0.2$ for $\varepsilon = 1/6, 1/15, 1/30$ (top to bottom) with Coulomb potential.

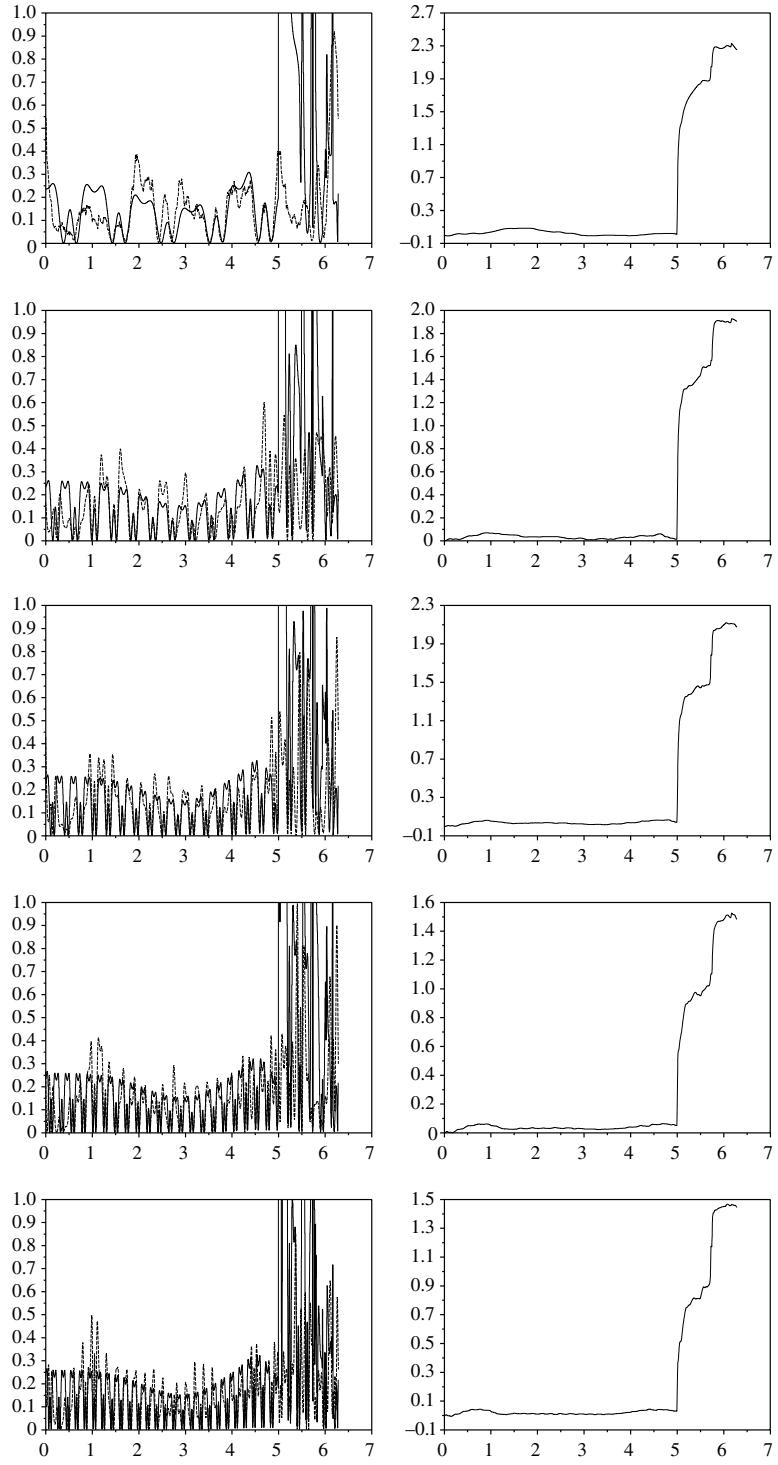

Fig. 15. Comparison $\rho^{\varepsilon}_{\mathrm{WKB}}$ (truncated, solid) vs. $|\psi^{\varepsilon}|^2$ (dotted) (left) and weak consistency (50) (right) at $T = 1.5$ for $\varepsilon = 1/6, 1/15, 1/21, 1/27, 1/33$ (top to bottom).

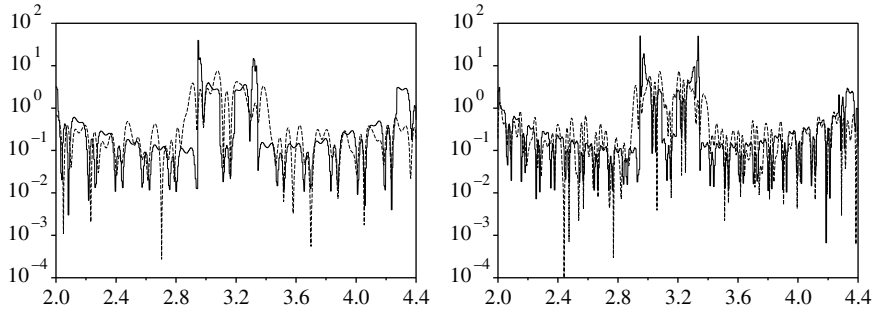

Fig. 16. Comparison $\rho^{\varepsilon}_{\mathrm{WKB}}$ (solid) vs. $|\psi^{\varepsilon}|^2$ (dotted) in logarithmic scale for $\varepsilon = 1/35, 1/65$ (left to right) with quadratic potential and $T = 1.5$.

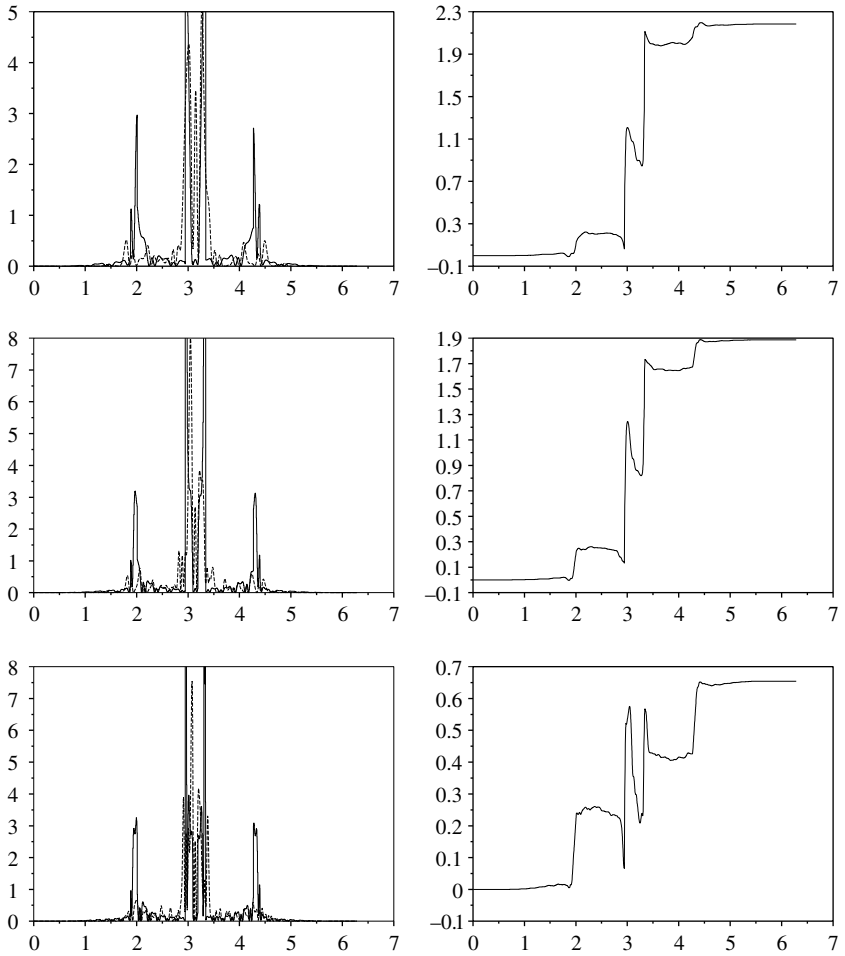

Fig. 17. Comparison $\rho^{\varepsilon}_{\mathrm{WKB}}$ (solid) vs. $|\psi^{\varepsilon}|^2$ (dotted) (left) and weak consistency (50) (right) in $T = 1.5$ for $\varepsilon = 1/15, 1/25, 1/35$ (top to bottom) with quadratic potential.

obtained with a coarser computational grid $\Delta x = \Delta t = 2\pi/1024$. We compare it to $|\psi^\varepsilon(T,\cdot)|^2$ at times $T = 0.2$ (no singularity) and $T = 1.5$ (two cusps) see Fig. 10). We observe on both Figs. 14 and 15 a behaviour similar to the one we saw in the preceding subsection for homogeneous problems; the intervals of variation for the function (50) are much bigger beyond caustic onset, see Fig. 15. It also looks like if the WKB approximation was a sort of "space average" of the more peaked Schrödinger solution, see especially Fig. 14. In particular, this figure reveals the behaviour of the time-splitting Fourier scheme in a situation where strong convergence as $\varepsilon \to 0$ is well-known. We finally stress that reaching a clear consistency result is not a simple task because the initial data (48) are already a bit noisy since the modulations z_κ are not known analytically. Further, the energy bands are still approximations obtained out of the numerical diagonalization of (16) and small errors are likely to propagate inside the moment systems (25) and the scheme (27). At last, the Fourier schemes may generate other kinds of errors from the noisy initial data and the (tacitly assumed) periodic boundary conditions; all of these have few reasons to compensate exactly. The use of a Krasny filer [2,14], can be of some help. The situation of the free Schrödinger equation investigated in [26] is much easier in the sense that the initial WKB ansatz is known analytically and the Fourier scheme is exact up to the very small `fft` errors.

6.3. Nonhomogeneous case: the quadratic potential

For the sake of completeness, we apply the preceding technique to carry out comparisons with the harmonic oscillator case already studied in Section 4.2. Results are shown in Fig. 16 in logarithmic scale and 17. The strong caustics are easily seeable in the WKB approximation; they are located inside a region where the Schrödinger solution varies highly itself. The intervals of variation for (50) decrease again with ε despite they are again quite big compared to the homogeneous case, compare with Fig. 11. The inadequation of the classical WKB method on caustics is very apparent on these graphs since, there, the error dominates completely. This means in particular that one still can not expect any monotonic decay of the L^1 norm of (50) as ε is decreased, even if the weak consistency looks rather satisfying on Fig. 17.

7. Conclusion and outlook

We have presented in this paper an algorithm to compute the semiclassical-homogenization limit of Schrödinger's equation (2) including commonly encountered exterior potentials. The two main difficulties are the indeterminacy of the energy bands, which must be used to compute numerical fluxes, and the recovery of the intensities, which is done relying on energy's conservation along Hamiltonian trajectories, see (32). Together with previous techniques [29], this allows to reconstruct "multiphase WKB observables" of the type (49) which appear to be quite consistent with the solution of linear Schrödinger's equation. However, this framework is somewhat limited in the sense that it completely discards the interactions of electrons with each other. As is well-known, the mean-field approximation of (5) is given by the Schrödinger–Poisson (Hartree) equation. In our 1D context which essentially models particular systems endowed with translational invariance in 2 directions, it reads

$$\mathrm{i}\hbar\partial_t\psi + \frac{\hbar^2}{2m}\partial_{xx}\psi = e(V(x) + eU(t,x))\psi, \qquad x \in \mathbb{R}, \tag{52}$$

where V still stands for the periodic potential of the lattice, but U is given by the self-consistent Poisson's equation:

$$-\epsilon_0\partial_{xx}U(t,x) = |\psi(t,x)|^2 - d(x),$$

and $d(x)$ is the *doping profile*, that is, the concentration of impurities in the crystal. It has been very recently shown, cf., [4], that for a medium's dielectric permittivity $\epsilon_0 = 1$ and $\hbar = m = 1$, the semiclassical limit of this system is given by the Vlasov–Poisson problem for $f(t,x,\xi)$:

$$\partial_t f + E'(\xi)\partial_x f - \left(D(x) - \int^x \int_{\mathbb{R}_\xi} f \,\mathrm{d}\xi \,\mathrm{d}x' \right) \partial_\xi f = 0, \tag{53}$$

with $D(x)$ being an antiderivative of the doping profile. A new *nonlinear* term arises: hence it is not clear whether the superposition principle can still be expected to hold in this case. This question will be investigated in details in the forthcoming Part 3 of this research.

Appendix A. One difficulty for the Schrödinger–Poisson system

From [4], we know that the problem (52) admits as its semi-classical limit the Vlasov–Poisson equation (53) for initial data belonging to the convenient energy band, see Theorem 4.2 in [4] for the precise statement. Indeed, the (formal) WKB equations coming from (52) read

$$\partial_t \varphi + E(\partial_x \varphi) + U(t,x) = 0, \qquad \partial_t \mu + \partial_x (E'(\partial_x \varphi)\mu) = 0, \tag{A.1}$$

for which characteristics solve a somewhat simple differential system because in 1D and if the effect of the orthonormal modulations z_κ^n is neglected, the electric field satisfies $F(t,x) = -\partial_x U(t,x) = \int^x \mu(t,s)\,\mathrm{d}s$ and thus solves a transport equation:

$$F(t,x) = \int^x \mu(t,s)\,\mathrm{d}s \Rightarrow \partial_t F + E'(u)\partial_x F = 0, \qquad u = \partial_x \varphi.$$

This precisely implies that it remains constant along characteristics. Solutions of (53) without doping profile $d(x) \equiv 0$ which remain monokinetic [37] correspond to the following Cauchy problem:

$$\begin{cases} X(t=0) \in \mathbb{R}, U(0,X(0)) = \partial_x \varphi_0(X(0)), F(0,X(0)) = \int^{X(0)} \mu_0(x)\,\mathrm{d}x, \\ \dot{X}(t) = E'(U(t,X(t))), \qquad \dot{U}(t,X(t)) = F(t,X(t)), \qquad \dot{F}(t,X(t)) = 0. \end{cases} \tag{A.2}$$

If one assumes furthermore the parabolic band approximation $E(U) = U^2/2m^*$, (A.2) admits the explicit solution: $\forall t > 0$, $F(t,X(t)) = F(t=0,X(0))$ and

$$X(t) = X(0) + \frac{t}{m^*} U(0,X(0)) + \frac{t^2}{2m^*} F(0,X(0)), \quad U(t,X(t)) = U(0,X(0)) + t.F(0,X(0)).$$

The feature that $t \mapsto F(t,X(t))$ remains constant allows to both integrate (A.2) and to produce a simple algorithm to generate *smooth* solutions of (A.1), see [37], relying on the ideas presented in this paper. However, this approach is not valid beyond breakup time because one must instead consider $F(t,x) = \sum_{k=1}^K \int^x \mu_k(t,s)\,\mathrm{d}s$, which expresses the fact that each of the K branches of solution is subject to the same overall electric field (independent of ξ in (53)). This feature is not reflected inside (A.2) so another algorithm is needed in order to study numerically the semiclassical limit of (52).

References

[1] N.W. Ashcroft, N.D. Mermin, Solid-State Physics, Rinehart and Winston, Holt, 1976.
[2] W.Z. Bao, Shi Jin, P.A. Markowich, On time-splitting spectral approximations for the Schrödinger equation in the semiclassical regime, J. Comp. Phys. 175 (2002) 487–524.

[3] C. Bardos, L. Erdös, F. Golse, N. Mauser, H.-T. Yau, Derivation of the Schrödinger–Poisson equation from the quantum N-body system, C.R. Acad. Sci. Paris I 334 (2002) 515–520.
[4] P. Bechouche, N. Mauser, F. Poupaud, Semiclassical limit for the Schrödinger–Poisson equation in a crystal, Comm. Pure Appl. Math. 54 (2001) 851–890.
[5] M. Ben Dahan, E. Peik, J. Reichel, Y. Castin,, C. Salomon, Bloch oscillations of atoms in an optical potential, Phys. Rev. Lett. 76 (1996) 4508.
[6] A. Bensoussan, J.L. Lions, G. Papanicolaou, Asymptotic Analysis for Periodic Structures, North-Holland, Amsterdam, 1978.
[7] M. Berry, Proc. R. Soc. Lond. A 392 (1984) 45.
[8] F. Bloch, Über die Quantenmechanik der Electronen in Kristallgittern, Z. Phys. 52 (1928) 555–600.
[9] F. Bouchut, S. Jin, X. Li, Numerical approximations of pressureless and isothermal gas dynamics, SIAM J. Numer. Anal. 41 (2003) 135–158.
[10] M. Brassart, Limite semi-classique de transformee de Wigner dans des milieux periodiques ou aleatoires Ph.D. thesis, Univ. de Nice, France, 2002.
[11] Y. Brenier, Averaged multivalued solutions for scalar conservation laws, SIAM J. Numer. Anal. 21 (1984) 1013–1037.
[12] Y. Brenier, L. Corrias, A kinetic formulation for multibranch entropy solutions of scalar conservation laws, Ann. I.H.P. Nonlinear Anal. 15 (1998) 169–190.
[13] Y. Brenier, E. Grenier, Sticky particles and scalar conservation laws, SIAM J. Numer. Anal. 38 (1998) 2317–2328.
[14] R.E. Caflish, T.Y. Hou, J. Lowengrub, Almost optimal convergence of the point vortex method for vortex sheets using numerical filtering, Math. Comput. 68 (1999) 1465–1496.
[15] R. Carles, P. Markowich, C. Sparber, Semiclassical asymptotics for weakly nonlinear Bloch waves, J. Stat. Phys, to appear.
[16] L.-T. Cheng, H. Liu, S.J. Osher, High-frequency wave propagation in Schrödinger equations using the level set method, Comm. Math. Sci. 1 (2003) 593–621.
[17] Marie C. Concordel, Periodic homogenization of Hamilton–Jacobi equations: Additive eigenvalues and variational formula, Indiana Univ. Math. J. 45 (1996) 1095–1118.
[18] M.C. Concordel, Periodic homogenization of Hamilton–Jacobi equations. II. Eikonal equations, Proc. Roy. Soc. Edinburgh Sect. A 127 (1997) 665–689.
[19] M. Dimassi, J.C. Guillot, J. Ralston, Semiclassical asymptotics in magnetic Bloch bands, J. Phys. A 35 (2002) 7597–7605.
[20] B. Engquist, O. Runborg, Computational high frequency wave propagation, Acta Numer. 12 (2003) 181–266.
[21] W. Gautschi, Moments in quadrature problems, Comput. Math. Appl. 33 (1997) 105–118.
[22] P. Gérard, P.A. Markowich, N.J. Mauser, F. Poupaud, Homogenization limits and Wigner transforms, Comm. Pure Appl. Math. 50 (4) (1997) 323–379.
[23] M. Glück, A.R. Kolovsky, H.J. Korsch, Wannier–Stark resonances in optical and semiconductor superlattices, Phys. Rep. 366 (2002) 103.
[24] L. Gosse, A well-balanced flux splitting scheme designed for hyperbolic systems of conservation laws with source terms, Comp. Math. Appl. 39 (2000) 135–159.
[25] L. Gosse, Using K-branch entropy solutions for multivalued geometric optics computations, J. Comp. Phys. 180 (2002) 155–182.
[26] L. Gosse, A case study on the reliability of multiphase WKB approximation for the one-dimensional Schrödinger equation, preprint (2004).
[27] L. Gosse, F. James, Convergence results for an inhomogeneous system arising in various high frequency approximations, Numer. Math. 90 (2002) 721–753.
[28] L. Gosse, S. Jin, X. Li, Two moment systems for computing multiphase semiclassical limits of the Schrödinger equation, Math. Models Meth. Appl. Sci. 13 (2003) 1689–1723.
[29] L. Gosse, P.A. Markowich, Multiphase semiclassical approximation of an electron in a one-dimensional crystalline lattice – I. Homogeneous problems, J. Comp. Phys. 197 (2004) 387–417.
[30] J.C. Guillot, J. Ralston, E. Trubowitz, Semiclassical asymptotics in solid-state physics, Comm. Math. Phys. 116 (1988) 401–415.
[31] F. Hövermann, H. Spohn, S. Teufel, Semiclassical limit for the Schrödinger equation for a short scale periodic potential, Comm. Math. Phys. 215 (2001) 609–629.
[32] S. Izumiya, G.T. Kossioris, Geometric singularities for solutions of single conservation laws, Arch. Rational Mech. Anal. 139 (1997) 255–290.
[33] Shi Jin, X. Li, Multi-phase computations of the semiclassical limit of the Schrödinger equation and related problems: Whitham vs. Wigner, Physica D 182 (2003) 46–85.
[34] Shi Jin, S. Osher, A level set method for the computation of multivalued solutions to quasi-linear hyperbolic PDEs and Hamilton–Jacobi equations, Comm. Math. Sci. 1 (2003) 575–591.
[35] J.B. Keller, Semiclassical mechanics, SIAM Rev. 27 (1985) 485–504.
[36] R. Kronig, W.G. Penney, Quantum mechanics of electrons in crystal lattices, Proc. Royal Soc. A 144 (1931) 101.
[37] H. Liu, E. Tadmor, Semilclassical limit of the non-linear Schrödinger–Poisson equation with subcritical initial data, Meth. Appl. Anal. 9 (2002) 517–531.

[38] V.G. Lyssenko, G. Valuis, F. Loser, T. Hasche, K. Leo, M.M. Dignam, K. Kohler, Direct measurement of the spatial displacement of Bloch-Oscillating electrons in semiconductor superlattices, Phys. Rev. Lett. 79 (1997) 301.
[39] P. Markowich, N.J. Mauser, F. Poupaud, A Wigner-function approach to semiclassical limits: electrons in a periodic potential, J. Math. Phys. 35 (1994) 1066–1094.
[40] P.A. Markowich, P. Pietra, C. Pohl, Numerical approximation of quadratic observables of Schrödinger-type equations in the semiclassical limit, Numer. Math. 81 (1999) 595–630.
[41] G. Nenciu, Dynamics of band electrons in electric and magnetic fields: rigorous justification of effective Hamiltonians, Rev. Mod. Phys. 63 (1991) 91–127.
[42] Q. Niu, X.-G. Zhao, G.A. Georgakis, M.G. Raizen, Atomic Landau–Zener tunneling and Wannier–Stark ladders in optical potentials, Phys. Rev. Lett. 76 (1996) 4504–4507.
[43] F. Poupaud, C. Ringhofer, Semi-classical limits in a crystal with external potentials and effective mass theorems, Comm. Partial Differenatial Equations 21 (1996) 1897–1918.
[44] O. Runborg, Some new results in multiphase geometrical optics, Math. Mod. Numer. Anal. 34 (2000) 1203–1231.
[45] G.M. Sklyar, L.V. Fardigola, The Markov power moment problem in problems of controllability and frequency extinguishing for the wave equation on a half-axis, J. Math. Anal. Appl. 276 (2002) 109–134.
[46] C. Sparber, P. Markowich, N. Mauser, Multivalued geometrical optics: Wigner functions vs. WKB methods, Asymptotic Anal. 33 (2003) 153–187.
[47] W.W. Symes, J. Qian, A slowness matching Eulerian method for multivalued solutions of Eikonal equations, J. Sci. Comp. 19 (2003) 501–526.
[48] G. Talenti, Recovering a function from a finite number of moments, Inverse Problems 3 (1987) 501–517.
[49] G.H. Wannier, Possibility of a Zener effect, Phys. Rev. 100 (1955) 1227–1236.
[50] C. Zener, A theory of electric breakdown of solid dielectrics, Proc. R. Soc. Lond. Ser. A 145 (1932) 523–529.